# A multiscale method for simulating fluid interfaces covered with large molecules such as asphaltenes

Åsmund Ervik[a,*], Morten Olsen Lysgaard[b], Carmelo Herdes[d], Guadalupe Jiménez-Serratos[c], Erich A. Müller[c], Svend Tollak Munkejord[e], Bernhard Müller[a]

[a] *Department of Energy and Process Engineering, NTNU, NO-7491 Trondheim, Norway*
[b] *Department of Mathematics, NTNU, NO-7491 Trondheim, Norway*
[c] *Department of Chemical Engineering, Imperial College London, London SW7 2AZ, United Kingdom*
[d] *Department of Chemical Engineering, University of Bath, Claverton Down, Bath, Somerset BA2 7AY, United Kingdom*
[e] *SINTEF Energy Research, P.O. Box 4761 Sluppen, NO-7465 Trondheim, Norway*

**Abstract**

The interface between two liquids is fully described by the interfacial tension only for very pure liquids. In most cases the system also contains surfactant molecules which modify the interfacial tension according to their concentration at the interface. This has been widely studied over the years, and interesting phenomena arise, e.g. the Marangoni effect. An even more complicated situation arises for complex fluids like crude oil, where large molecules such as asphaltenes migrate to the interface and give rise to further phenomena not seen in surfactant-contaminated systems. An example of this is the "crumpling drop" experiments, where the interface of a drop being deflated becomes non-smooth at some point. In this paper we report on the development of a multiscale method for simulating such complex liquid-liquid systems. We consider simulations where water drops covered with asphaltenes are deflated, and reproduce the crumpling observed in experiments. The method on the nanoscale is based on using coarse-grained molecular dynamics simulations of the interface, with an accurate model for the asphaltene molecules. This enables the calculation of interfacial properties. These properties are then used in the macroscale simulation, which is performed with a two-phase incompressible flow solver using a novel hybrid level-set/ghost-fluid/immersed-boundary method for taking the complex interface behaviour into account. We validate both the nano- and macroscale methods. Results are presented from nano- and macroscale simulations which showcase some of the interesting behaviour caused by asphaltenes affecting the interface. The molecular simulations presented here are the first in the literature to obtain the correct interfacial orientation of asphaltenes. Results from the macroscale simulations present a new physical explanation of the crumpled drop phenomenon, while highlighting shortcomings in previous hypotheses.

*Keywords:*

## 1. Introduction

Interfacial tension is a remarkable phenomenon, in that the tumultuous interactions of fluid molecules of different types and shapes give rise to macroscopic interfaces being not only smooth and stable, but indeed well-described by a single material constant, viz. *the interfacial tension* $\gamma$. This holds true for an impressive number of fluid molecules that may be polar or non-polar and may have different topology and size. It is by adding a third phase to the system, this phase being interfacially active either by virtue of amphiphilicity or

*Corresponding author
*Email addresses:* asmunder@pvv.org (Åsmund Ervik), morten@lysgaard.no (Morten Olsen Lysgaard), c.e.herdes.moreno@bath.ac.uk (Carmelo Herdes), m.jimenez-serratos@imperial.ac.uk (Guadalupe Jiménez-Serratos), e.muller@imperial.ac.uk (Erich A. Müller), svend.t.munkejord@sintef.no (Svend Tollak Munkejord), bernhard.muller@ntnu.no (Bernhard Müller)

through being poorly soluble in either fluid, that more complicated dynamics arise. The simplest case is that of amphiphilic surfactant molecules, where Marangoni [1, 2] first described the effects of nonuniform interfacial tension, and Gibbs in his seminal treatise [3] was the first to consider the effective elasticity of the interface imparted by the surfactants. The first mention of the deliberate use of surfactants to alter the interfacial properties of liquids is, however, much earlier. In book two of Pliny the Elder's encyclopedic *Naturalis Historia* [4, 5] (77 AD) it is mentioned that divers would release small oil drops from their mouth, to smooth the surface of the sea and thus increase the amount of light transmitted down to them.

Even though surfactants give rise to richer dynamics, their effects can be modelled using simple equations dependent on macroscopic parameters, using the approaches developed by Gibbs [3], Pockels [6], Szyszkowski [7], Langmuir [8] and Frumkin [9] (among others); see Levich and Krylov [10] (or the book by Levich [11]) for a good introduction. Apart from studies using these approaches for systems with low surfactant concentration, there is also a rich field of study into the various phases and phase transitions in the three-component systems when the number of surfactant molecules becomes comparable to the number of fluid molecules. However, we will not discuss this in further detail here. In the end, the effect of surfactants at low concentration is an interfacial tension which may vary along the interface, according to the variation in interfacial concentration of the surfactant. The relation between concentration and interfacial tension is given by e.g. a Langmuir equation of state.

In more recent years, as experimental techniques have increased in sophistication and soft matter has come to be a field of its own, attention has also turned to larger molecules at fluid interfaces. These larger molecules may originate from biological systems, being e.g. proteins or lipids, or they may originate from complex fluids such as crude oil, for instance asphaltenes. These molecules cause effects beyond those seen in surfactant systems, e.g. the crumpling upon deflation of red blood cells [12] or asphaltene-covered drops [13, 14]. It follows that something more than a (possibly varying) interfacial tension appears in these systems. We shall focus our attention here on asphaltenes, and will use this term rather than "large molecules" for the remainder of the paper, but the method remains general.

Let us then consider the asphaltenes. Having earned a reputation as the "cholesterol of crude oil", this component causes many problems in petroleum extraction, processing and refinement. As the name suggests, asphaltenes are similar in appearance to asphalt, and are found in large quantities in bitumen, but are present to some degree in most crude oils. The first reported discussion of asphaltenes is by Boussingault [15] who coined the term in 1836 (see Hoepfner [16, Chapter 1.1] for a historical review) but there is still today disagreement about their properties. Indeed, there was debate in the literature [17] up until recently on what their average molecular weight is. Furthermore, the precise definition of what constitutes an asphaltene is still not agreed upon. A commonly used operational definition is that it is the part of crude oil which is soluble in toluene but insoluble in $n$-heptane, as codified e.g. in the ASTM D 6560 – 00 standard. (From here on, we will denote $n$-heptane simply by heptane; branched alkanes are not considered in this work.) But this definition in terms of solubilities is more a description of how to isolate asphaltenes in the laboratory, as opposed to a definition of what they are.

The case is not clearer from the molecular perspective, as advanced experimental techniques such as neutron scattering or high-resolution mass spectrometry [18] have shown that there are thousands of different empirical formulae in a given asphaltene sample. Samples from different oil fields around the world have different asphaltene compositions. Furthermore, since asphaltenes have of the order of 50 carbon atoms, even for a single empirical formula the number of isomers is in the trillions. One may compare asphaltene molecules to snowflakes; no two are exactly the same. It has been argued that asphaltenes are among the most complex materials ever studied [16].

The effect of asphaltenes on liquid-liquid interfaces is also complicated. One such effect is that they make it hard to separate emulsions of water and crude oil. See e.g. Jones et al. [19], Gafonova and Yarranton [20], Sjöblom [21], Kokal [22], Kilpatrick [23] for reviews on water-in-crude oil emulsion stability. Emulsion stability has been directly linked to the properties that the asphaltenes impart on the interface [24, 25]. The asphaltenes give rise to interesting phenomena such as the previously mentioned crumpled drops reported by Yeung et al. [13], Pauchard et al. [14].

In the present paper we report on our development of a multiscale method that enables the simulation of liquid-liquid interfaces covered with asphaltenes (or other large molecules). This multiscale method is loosely

coupled, with equilibrium simulations at the nanoscale providing parameters for dynamic simulations at the macroscale. Many classifications exist of multiscale methods, some of which have a much tighter coupling between the scales than in the present approach, see e.g. [26, 27] for reviews of multiscale methods.

The outline of this paper is as follows. In Section 2 we review the theory and present the methods used on the nanoscale and the macroscale, in particular the SAFT-$\gamma$ Mie approach to coarse-grained molecular dynamics simulation (Section 2.1), and the hybrid level-set/ghost-fluid/immersed-boundary method developed in this work for simulation of two-phase flows with complex interfaces(Section 2.4). The latter method is summarised in Section 3. Subsequently, in Section 4, we validate these methods using standard test cases for interface-capturing methods (Section 4.1), and by comparing the predictions from molecular simulations to experimental results (Section 4.2). We then present the results obtained with the method in Section 5, discuss the implications of these results in Section 6, and finally give some concluding remarks in Section 7.

## 2. Theory and methods

### *2.1. Nanoscale: theory*

The complicated behaviour of liquid-liquid interfaces contaminated with asphaltenes is caused by the interactions between the molecules at the interface. It is thus tempting to try and explain the interfacial phenomena by modelling the molecular interactions. These are, in turn, also complicated, and one is forced to make simplifications. On the most basic level, many-body quantum mechanics is what lies behind the nature and interactions of molecules. Fortunately, on the scale of interactions between large molecules, one may develop an effective theory which is much simpler. This theory has roots going back to the dawn of thermodynamics, when pioneering efforts were made to understand how the microscopic nature of fluids could explain their behaviour. The works by Maxwell, Boltzmann, van der Waals, Lennard-Jones, Mie, Chapman, Engskog and others paved the way to our understanding of simple fluids from the molecular perspective; see e.g. Chapman et al. [28] for an overview. For less simple fluids, it was not until the advent of computer simulations that the molecular perspective was able to provide some insights.

One of the major challenges in simulating the behaviour of chemicals comes from the need for good models that can accurately predict physical and chemical properties. For many simple substances, experimental data may already be available or easy to obtain. However, many interesting systems contain one or several chemically complex species, e.g. polymers, surfactants, and our asphaltenes. The quantitative prediction of the thermodynamic properties of such systems, especially their phase behaviour and mesoscopic structure, is very challenging. Simple equations of state are typically unable to make good predictions of the properties of structured fluids. As this much is clear, one must resort to computer simulations of these more complex fluids.

Many molecular simulation methods rely on force fields or other empirical parameters that are fitted to reproduce the properties of particular classes of compounds, or to a particular large data set. These methods may have trouble predicting the properties of complex mixtures. Truly *ab initio* prediction, using electronic structure methods, is possible only for very small systems and processes spanning very short time scales, and cannot be used directly to predict the properties of structured fluids or complex materials. It is possible to construct models for complex systems by first building models for the different (smaller) component parts using more predictive methods, and then eliminating the unimportant degrees of freedom.

This leads to a coarse-grained description that can be used to predict properties of more complex materials. However, it is time-consuming to generate the data for the smaller building blocks, and it is often not clear what the best way is when coarse-graining out the smaller/faster degrees of freedom. An alternative approach is to construct a coarse-grained model directly using experimental data for the building blocks ("top-down" coarse graining) – in this case the evaluation of the residual when performing the fit depends on a relatively costly simulation, making the cost of fitting very high.

Recently, however, an alternative approach has been successfully used to fit coarse-grained models to thermodynamic data without using simulations, but rather using statistical mechanical perturbation theory. This novel approach, the SAFT-$\gamma$ method, allows for the construction of coarse-grained models suitable for molecular simulation of complex fluids using available experimental data for the constituent blocks. The

SAFT equation of state is a perturbation approach based on a well-defined Hamiltonian. The reader is referred to several reviews on SAFT that describe the various stages of its development, up to the current SAFT-$\gamma$ Mie approach [29, 30, 31, 32, 33, 34]. In the current approach, a Mie [35] potential gives the forces between the coarse grained *beads* in the method,

$$V(r) = C(n,m)\,\epsilon\left[\left(\frac{\sigma}{r}\right)^{n} - \left(\frac{\sigma}{r}\right)^{m}\right], \tag{1}$$

$$C(n,m) = \left(\frac{n}{n-m}\right)\left(\frac{n}{m}\right)^{m/(n-m)}, \tag{2}$$

where $r$ is the distance between a pair of beads, and $\epsilon$ and $\sigma$ are the adjustable parameters relating to the energy and distance scales. Each bead typically corresponds to 2–4 atoms heavier than hydrogen, together with the hydrogen atoms attached to the heavier atoms. Referring to Figure 1, the parameter $\epsilon$ corresponds to the depth of the potential well, and $\sigma$ to the distance $r$ where the potential switches from being repulsive to being attractive. Thus $\sigma$ is taken to correspond to the bead "diameter" for visualisation purposes. Note that in the $n \to \infty$ limit, $V(r)$ becomes a hard-sphere potential with diameter equal to $\sigma$.

It is important to note that in the present approach, the attractive exponent $m$ is fixed at the value of six, but the short-range repulsion exponent $n$ takes on different values reflecting the average softness or hardness of the potential for a given molecule. The fact that $m = 6$ is fixed is due to the observation that these two exponents are not independent parameters [36], so fixing one simplifies the parameter space considered. The effect of varying $n$ is illustrated in Figure 1 where the potential is plotted for $n$ ranging from 8 to 24 in steps of 2. The $n = 12$ or Lennard-Jones potential is shown in a stronger orange colour. It is seen that allowing $n$ to vary allows for using softer or harder potentials for beads representing different molecules, which is something that cannot be achieved in many other approaches which rely on only the Lennard-Jones potential.

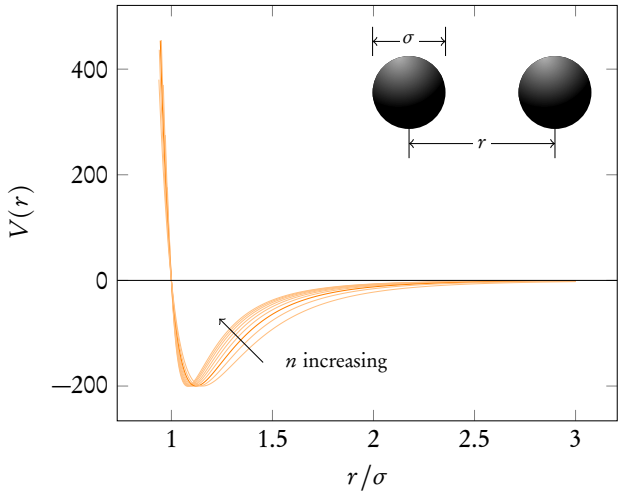


Figure 1: The Mie (m,6) potential shown for $\epsilon = 200$ (in arbitrary units) and $n$ varying from 8 to 24, as a function of the dimensionless distance $r/\sigma$. The Lennard Jones (12,6) potential is shown in a stronger colour. In the corner, the two beads are illustrated with a distance $r$ and a "diameter" $\sigma$.

There are several methodologies proposed in the literature to obtain parameters for coarse grained models [37] . Most common approaches start from a fine-detailed model, usually an atomistically-detailed characterization and integrate out degrees of freedom which are deemed unessential [38]. This procedure, known as a bottom-up approach, inevitably discards information and produces potentials which can rarely be used in states points other than those used to develop them.

A pathway to circumvent these problems is to employ a top-down or thermodynamic approach, where the force field of the coarse grained sectors is an effective or average potential capable of reproducing

macroscopic thermodynamic properties. These top-down coarse grained models provide by their own nature parametrizations which are usually robust, representative or transferrable. Two notable examples are the MARTINI force field [39, 40], which employs a group contribution approach targeted at biomolecular simulations where uniform-sized coarse grained beads have been fitted to water/octanol solubilities.

In a group contribution approach, molecules which have different parts with different properties are modelled using combinations of beads which represent each individual part. As an example, octanol could be modelled with one bead that represents the head with the alcohol group, based on the thermophysical properties of ethanol, and the other beads which represent the aliphatic tail could be based on the properties of hexane.

A more refined coarse-grained model is the SAFT-$\gamma$ force field [41], which employs an analytical equation of state as the bridge between macroscopic thermophysical properties and the underlying intermolecular potential that can effectively generate them. The most direct method of parametrization of coarse grained segments and chemical moieties is to use the appropriate version of the SAFT equation of state to fit experimental phase equilibria data, e.g. saturated liquid densities, vapour pressures, etc. essentially equating the free energy of a coarse grained model to that obtained from the analysis of experimental data [42, 43, 33, 44].

However, if one recognizes the conformal nature of the underlying Mie potential, one can formulate the equation of state in terms of a corresponding-states model and can express the properties of any non-associating fluid in terms of a finite set of defining properties: a critical temperature, the acentric factor and a well-defined density. This approach [45] greatly simplifies the parameter estimation without detriment to the robustness of the methodology, as exemplified by the predictions of adsorption [46], transport and interfacial properties [41] which are not part of the original fit, and the description of complex molecules such as surfactants [47, 48], resins and asphaltenes [49]. This approach is used to construct the force field parameters used in this work. The parameters for different coarse-grained beads are given in Appendix B.

### *2.2. Nanoscale: numerical methods*

Once the parameters for the intermolecular force field have been established for all molecules under consideration, one can proceed to study the system. Since only the two-bead problem has an analytical solution, a numerical approach is required for any realistic system. There are two fundamental approaches, namely Monte Carlo methods and Molecular Dynamics (MD) methods. The ergodic hypothesis asserts that these two are the same, i.e. that ensemble averages and time averages give the same answers. Molecular dynamics is the approach used in this work, so we will not discuss Monte Carlo methods in any detail.

In molecular dynamics, the equations of motion are solved to evolve the system in time from some initial state. The equations of motion are Newton's second law for each of the $N$ beads in the system, with the force given by the Mie potential in the approach used here. Denote by $\mathbf{x}_i$ the position of bead $i$ with mass $m_i$. The equations of motion are then

$$\frac{\partial^2 \mathbf{x}_i}{\partial t^2} = \sum_{j \neq i} \frac{F(|\mathbf{x}_j - \mathbf{x}_i|)}{m_i} \frac{\mathbf{x}_j - \mathbf{x}_i}{|\mathbf{x}_j - \mathbf{x}_i|} \tag{3}$$

where the forces are assumed to be conservative, and depending only on the distance between two beads. Thus the forces are given by a potential $V(r)$. This must be specified; a Mie potential is used here, as discussed previously. This potential is short-ranged, so a *cutoff* $r_{\text{cut}}$ is specified, beyond which $V(r) = 0$. The equations of motion are solved numerically using a symplectic integration method, since this ensures the simulation is stable over long times and that the energy drift is very small. An example of such a method is the velocity Verlet method. Here, the velocities $\mathbf{v}_i$ and positions $\mathbf{x}_i$ are stored at each time step $n$. The

system is integrated forward in time to the time step $n+1$, with a step length $\Delta t$, according to

$$\mathbf{v}_i^{n+1/2} = \mathbf{v}_i^n + \sum_{j \in \mathbb{N}(i,n)} \frac{\Delta t}{2m} F(|\mathbf{x}_j^n - \mathbf{x}_i^n|) \frac{\mathbf{x}_j^n - \mathbf{x}_i^n}{|\mathbf{x}_j^n - \mathbf{x}_i^n|} \tag{4}$$

$$\mathbf{x}_i^{n+1} = \mathbf{x}_i^n + \mathbf{v}_i^{n+1/2} \Delta t \tag{5}$$

$$\mathbf{v}_i^{n+1} = \mathbf{v}_i^{n+1/2} + \sum_{j \in \mathbb{N}(i,n+1)} \frac{\Delta t}{2m} F(|\mathbf{x}_j^{n+1} - \mathbf{x}_i^{n+1}|) \frac{\mathbf{x}_j^{n+1} - \mathbf{x}_i^{n+1}}{|\mathbf{x}_j^{n+1} - \mathbf{x}_i^n|} \tag{6}$$

Here $\mathbb{N}(i,n)$ is the neighbourlist of bead $i$, i.e. the indices of all beads which are within the cutoff distance of bead $i$ at the time step $n$. Using a neighbourlist dramatically speeds up the algorithm, but comes at a storage cost; this data structure accounts for the bulk of the memory used by a molecular dynamics code. The fact that all interactions are local makes the method well-suited for parallelisation, both on classical CPUs and on accelerators such as graphical processing units (GPUs).

The beads are contained in a virtual simulation box, typically with periodic boundary conditions. The initial state must be generated somehow. In the present work we start from random initial conditions at a low density. To go from this initial state to the desired system state, e.g. a temperature $T$ and a pressure $p$, the system is evolved in the isothermal-isobaric or $NpT$ ensemble, where a thermostat and a barostat are employed to adjust the bead velocities and the simulation box size, respectively, to obtain the desired system state. Once this state is reached, the simulation box size is fixed and the system is subsequently evolved in the canonical or $NVT$ ensemble. The reader is referred to standard textbooks on molecular dynamics, e.g. by Allen and Tildesley [50], Frenkel and Smit [51], for further details.

While the first molecular dynamics simulations [52, 53] were limited to two-dimensional systems and simple potentials, the results obtained provided fascinating new insights into the molecular world. With the exponential increase in computing power since the 1950's, molecular dynamics simulations today have probed systems with hundreds of billions of atoms [54], or entire virus capsules [55], using large high-performance computing systems.

Combining a coarse-grained approach to molecular dynamics, such as the SAFT-$\gamma$ Mie force field used here, with the power of general purpose GPUs, we obtain speedups of more than three orders of magnitude over atomistically detailed simulations running on usual CPUs [56]. This means the present simulations, even though they evolve systems with about one million atoms for hundreds of millions of timesteps in total, are run on computational resources that can fit inside a desktop computer. The simulations reported here are run in parallel typically on two or four GPUs; separate simulations are run simultaneously on different nodes of a GPU cluster, consuming in total 8000 GPU-hours during this study.

For coarse-grained molecular dynamics simulations we employ our raaSAFT code [56], a framework for simulations using the SAFT-$\gamma$ Mie force field. raaSAFT leverages existing molecular dynamics codes to do the heavy lifting. Here HOOMD-blue [57, 58] is used, a modern GPU-first code that shows excellent performance and scalability on multiple GPUs.

HOOMD-blue takes a conservative approach to molecular dynamics, and uses algorithms that do not sacrifice accuracy for speed. The simulations are run in the isothermal-isobaric ($NpT$ ) or the isothermal-isochoric ($NVT$ ) ensemble, and the system is evolved in these ensembles using the Martyna-Tobias-Klein approach [59]. This approach gives dynamics that are provably time-reversible and energy-preserving. In the light of this, it is interesting how the simulations show time-irreversible results, such as the clustering of asphaltenes. This is a variant of Loschmidt's paradox. Recent work by Hoover et al. [60, 61, 62] might provide some insight into the explanation of this, but so far it appears to remain an open question.

When systems with immiscible fluids are considered, it is of interest to compute the interfacial tension. To do this, the simulation box is elongated in one direction, and this asymmetry causes the formation of interfaces along the two shorter dimensions of the box, since this minimises the free energy of the interfaces. Note that since periodic boundary conditions are employed, it is a topological impossibility to have an odd number of interfaces between two liquids, so the desired system state has two slabs of liquid which are in contact at two interfaces.

For this system, we may compute the interfacial tension from the integral of the anisotropy in the diagonal elements of the stress tensor, $\sigma_{ii}$, along the elongated box dimension. To be precise, assuming the box is elongated in the $z$-direction where the box dimension is $L_z$, the interfacial tension is given by

$$\gamma = \frac{L_z}{2} \int_0^{L_z} \left( -\sigma_{zz} + \frac{1}{2}(\sigma_{xx} + \sigma_{yy}) \right) dz. \tag{7}$$

This is referred to as the mechanical route to the interfacial tension, and goes back to Kirkwood and Buff [63]. For a comparison of this with alternative methods, see e.g. [64]. Note that the integral here can be split into three parts, so molecular dynamics software such as HOOMD-blue typically compute the values

$$p_{xx} = \int_0^{L_x} -\sigma_{xx} dx, \tag{8}$$

and similarly for $p_{yy}, p_{zz}$, and refer to these as the diagonal components of the "pressure tensor". From these three numbers we may compute the interfacial tension using Equation (7). Since molecular dynamics simulations are inherently noisy, in particular for properties related to the pressure, $\gamma$ computed from this expression for a single point in time will fluctuate significantly from one time step to the next. To obtain a reliable value for $\gamma$, time averages must be employed.

To also compute the elasticity of the interface, we follow refs. [65, 66], where the elasticity $K_a$ is computed from the change in interfacial tension $\Delta\gamma$ (as computed from Equation (7)) when the interfacial area is changed from $A_0$ to $A$, given by the expression

$$K_a = \frac{\Delta\gamma}{A/A_0 - 1}. \tag{9}$$

These two parameters, $\gamma$ and $K_a$, are subsequently employed as material parameters in the macroscale simulations.

### *2.3. Macroscale: theory*

The flow inside and around water drops in oil behaves according to the incompressible Navier-Stokes equations. For a derivation of these and a general overview, the reader is referred to standard textbooks e.g. by Batchelor [67] or Lamb [68]. The incompressible Navier-Stokes equations for single-phase flow read

$$\rho \left( \frac{\partial \mathbf{u}}{\partial t} + \mathbf{u} \cdot \nabla \mathbf{u} \right) = -\nabla p + \boldsymbol{\nabla} \cdot (\mu \boldsymbol{\nabla} \mathbf{u}) + \rho \mathbf{f}, \tag{10}$$

$$\nabla \cdot \mathbf{u} = 0, \tag{11}$$

$$\mathbf{u}(\mathbf{x}, 0) = \mathbf{u}_0(\mathbf{x}), \tag{12}$$

$$\mathbf{u}_{\partial\Omega}(t) = \mathbf{g}(t), \tag{13}$$

where $\partial\Omega$ is the domain boundary and $\mathbf{g}(t)$ is the velocity boundary condition. The initial condition is $\mathbf{u}_0$. The viscosity $\mu$ and the density $\rho$ are assumed to be constant throughout the domain. The velocity is denoted by $\mathbf{u}$ and the pressure by $p$, and $\rho\mathbf{f}$ is a body force such as gravity. This can be extended to handle two fluid phases, with different viscosities and densities. Let $\Omega_1$ and $\Omega_2$ denote the domains filled with fluid 1 and fluid 2, respectively and $\Gamma$ denote the interface separating the two fluids, i.e. we have $\Omega = \Omega_1 \cup \Omega_2$, as illustrated in Figure 2.

The tension on $\Gamma$ can be modelled as a contribution to Equation (10), localised at the interface. In this work we consider one-dimensional or axisymmetric two-dimensional interfaces, and in both cases the interface is parametrised as a one-dimensional curve $\mathbf{x}_I(s)$. In the axisymmetric case, this curve is swept around the azimuthal angle $\phi$ to form the two-dimensional interface. The interfacial tension has two contributions in the axisymmetric case, $T_s$ and $T_\phi$, both of which may vary as functions of the position $s$ along the interface. In the case of a one-dimensional interface, $T_\phi = 0$.

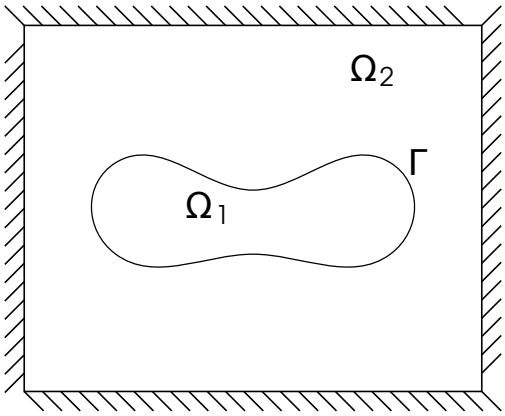


Figure 2: Two fluid phases, the inner fluid 1 in $\Omega_1$ and the outer fluid 2 in $\Omega_2$, and the interface $\Gamma$ separating them.

The interfacial force contribution to the body force in Equation (10) is then

$$\mathbf{f}_s(\mathbf{x},t) = \int_\Gamma \left( \frac{\partial T_s}{\partial s}\mathbf{t} + T_s\kappa_s\mathbf{n} + T_\phi\kappa_\phi\mathbf{n} \right) \delta(\mathbf{x}-\mathbf{x}_I(s))\mathrm{d}\mathbf{s}, \tag{14}$$

where $\frac{\partial T_s}{\partial s}$ is the derivative of the meridional tension along the interface, $\mathbf{t}$ is the interface tangent, $\kappa_s, \kappa_\phi$ are the curvatures, $\mathbf{n}$ is the principal unit normal vector, and $\delta$ is the Dirac delta function. We assume here that the interfacial curvature is small enough that the interface is approximately flat on the microscopic level. This is a good approximation for drops with radius $R \gg 1\text{nm}$ [69], which does not pose a significant restriction. The interfacial tension for pure fluids is then dependent just on the temperature and the pressure.

In Figure 3 we illustrate the tensions for the axisymmetric case, together with the two coordinate systems employed, on a spherical drop. Note that the drop is not restricted to being spherical, so none of the coordinate systems are spherical, and $s$ is an arc length, not an angle. The line parametrised by $s$, which represents the drop surface, actually lies in the $(r,z)$ plane, but in the figure the line is rotated out of the plane in order to avoid clutter. Since we assume axisymmetry, neither of the coordinate systems will have points discretising the $\phi$-direction in the numerical methods.

On the right-hand side of this figure, the tensions $T_s$ and $T_\phi$ are indicated as line segments in the directions of strain, using varying red and green colours, respectively. Both tensions may vary along the $s$-direction, but are constant in the $\phi$-direction since axisymmetry is assumed. As is indicated in Equation (30) in the next section, only the variation in $T_s$ can give rise to a tangential force. From the figure we understand this, since any non-normal component of the force caused by $T_\phi$ would have to be either in the azimuthal direction, violating the assumption of axisymmetry; or in the meridional direction, but this force would be binormal to the strain line, which is not possible.

The description of an interface between two fluids can be as simple as a constant interfacial tension $T_s = T_\phi = \gamma$, or more complicated due to molecules which are interfacially active. In any case, the formation of the interface gives an increase in the energy of the system, and we denote the energy density of the interface by $w$. It should be noted that while the interfacial energy (in $\mathrm{J/m^2}$) and the interfacial tension (in $\mathrm{N/m}$) are identical for the case of simple fluids, this is *not* the case for an interface with a more complicated interface which has elastic properties; see e.g. [70] for details.

Following [71], we write $w$ as a function[1] of the interfacial deformations $\lambda_s$ and $\lambda_\phi$,

$$w = w(\lambda_s, \lambda_\phi). \tag{15}$$

[1] $w$ is technically a functional; see e.g. [72] for a more mathematical formalism.

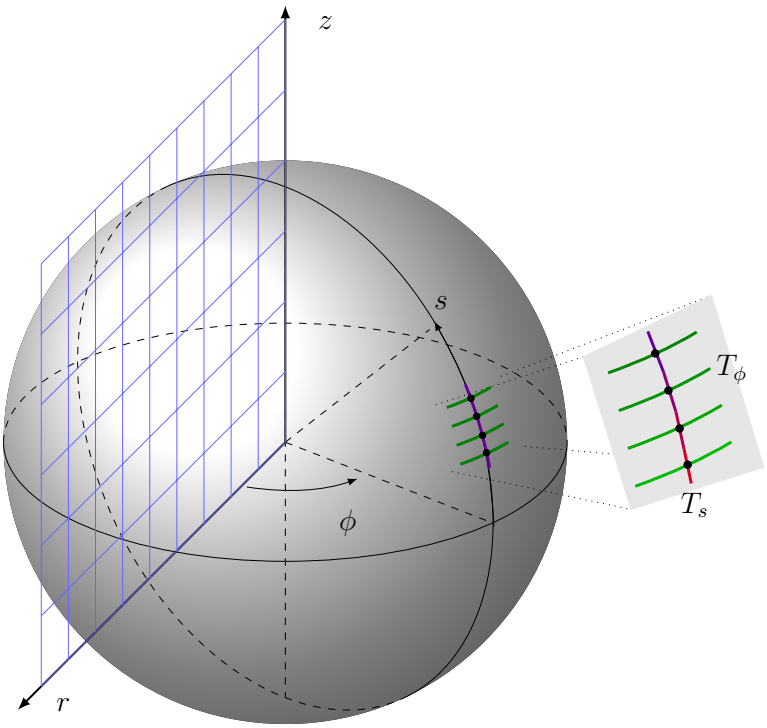


Figure 3: Illustration of the two coordinate systems employed, and the tensions on the drop. The blue grid illustrates the $(r, z)$ coordinate system, where a structured grid is employed and the Navier-Stokes equations are solved. The grey sphere illustrates the shape of a drop. On this drop, the coordinates $s, \phi$ are used. Note that $s$ is an arc length, not an angle. On the right, the tensions are illustrated with red ($T_s$) and green ($T_\phi$) line segments. The varying colours indicate varying tensions. Note that while both tensions vary from point to point, only $T_s$ varies in the direction parallel to the corresponding strain $\lambda_s$, while $T_\phi$ is constant in the direction parallel to $\lambda_\phi$ (due to axisymmetry).

These deformations refer to the length of an interfacial element $l_i$ at time $t$ relative to the undeformed length at $t = 0$, i.e. $\lambda_s = l_i(t)/l_i(0)$. The interface will tend to deform such that the energy is minimised, while maintaining a constant volume inside. The minimal energy shape depends on the form of $w$; for the familiar case of constant interfacial tension the minimal energy shape is a sphere.

We proceed to derive the general tensions for an interface which is described by a constant interfacial tension $\gamma$ and a Hookean elasticity $K_a$, following again [71]. The bending rigidity of the interface is assumed to be zero; a non-zero bending rigidity may be considered in future work. As noted previously, we parametrise the interface using the coordinate $s$ along the interface in the $(r, z)$ plane. All quantities in the system are constant along the azimuthal direction $\phi$. Under these assumptions the energy $w$ is given by

$$w = \frac{1}{2}\left[\frac{K_a}{1-\nu^2}\left((\lambda_s-1)^2 + 2\nu(\lambda_s-1)(\lambda_\phi-1) + (\lambda_\phi-1)^2\right) + \gamma\lambda_s\lambda_\phi\right]. \tag{16}$$

To obtain the tensions one takes the partial derivatives of the energy with respect to the deformations; to be precise,

$$T_s = \frac{1}{\lambda_\phi}\frac{\partial w}{\partial \lambda_s} = \frac{K_a}{\lambda_\phi(1-\nu^2)}\left(\lambda_s + \nu\lambda_\phi - (1+\nu)\right) + \gamma, \tag{17}$$

$$T_\phi = \frac{1}{\lambda_s}\frac{\partial w}{\partial \lambda_\phi} = \frac{K_a}{\lambda_s(1-\nu^2)}\left(\lambda_\phi + \nu\lambda_s - (1+\nu)\right) + \gamma, \tag{18}$$

$$\tag{19}$$

which are the tensions in the meridional and azimuthal directions, respectively. These are inserted into Equation (14) to obtain the force on the interface. In these expressions $\nu$ denotes the Poisson ratio, which is a material constant that couples the meridional and azimuthal deformations. In the present work, $\nu = 0.3$ is used, which is a reasonable assumption for elastic interfaces such as those considered here [73].

### *2.4. Macroscale: numerical methods*

Having described the equations governing the system, we now consider how to solve these numerically. For the numerical methods, the equations must be discretised in space and time. In space, a structured, uniform and staggered grid is employed, and the derivatives are discretised using standard second-order finite differences, except for the convective term in Equation (10) which is discretised using the fifth-order WENO scheme [74, 75]. Due to the coupling between pressure and velocity, the Navier-Stokes equations are not a regular set of PDEs, but technically a differential-algebraic equation with an index-2 constraint given by the incompressibility equation. To solve this, we employ the pressure projection method due to Chorin [76], which leads to a splitting scheme for the time integration. In this scheme, we solve first for an intermediate (non-divergence-free) velocity field using an Euler step, then solve a Poisson equation for the pressure based on this intermediate velocity, and finally use the computed pressure to project the velocity field into the space of divergence-free velocity fields. The pressure Poisson equation takes up the bulk of the computation time, and much work has gone into developing fast numerical methods for this equation. In the present work we employ the BoomerAMG [77] preconditioned BiCGStab [78] method, through the Hypre [79] and PETSc [80] libraries, respectively. To obtain a larger stability domain than with only an explicit Euler step, several Euler steps are combined to form a Runge-Kutta step (following the approach by Kang et al. [81]), specifically the SSP-RK(2,2) method is employed here (using the notation of Gottlieb et al. [82]). The method does, however, remain first-order in time due to the irreducible splitting error introduced by the projection step; see [83] for a review of error reduction and of higher-order projection methods for the Navier-Stokes equations.

This summarises how the single-phase Navier-Stokes equations are solved. To extend this to two-phase flow, several methods are available. In previous work we have employed the combination of the level-set and ghost-fluid methods, which gives results that agree well with theory and experiments [84, 85, 86, 87, 88, 89], and which can handle topological changes in the interface, e.g. during drop coalescence. This method can handle a varying interfacial tension, and has been coupled with the Langmuir equation of state to simulate the effects of insoluble surfactants [86, 89].

To simulate interfaces with tensions that include a Hookean elasticity, this scheme had to be extended, as we will discuss in the following. To this end, a hybrid level-set/ghost-fluid/immersed-boundary method has been developed. To describe the hybrid method, we first give a brief overview of each of the methods it is constructed from. The development of the hybrid method is documented in greater detail in the MSc thesis of Lysgaard [90] for the two-dimensional case; the method was extended to axisymmetry later.

#### *2.4.1. The level-set method*

To solve the Navier-Stokes equations for two-phase flow, knowledge of the interface is required. For this, a popular choice is the level-set method, originally proposed by Osher and Sethian [91]. With this method the interface is encoded as a signed scalar distance field

$$\varphi(\mathbf{x}, t) = \begin{cases} \min_{\mathbf{x}' \in \Gamma(t)} \|\mathbf{x} - \mathbf{x}'\| & \text{if } \mathbf{x} \in \Omega_1 \\ -\min_{\mathbf{x}' \in \Gamma(t)} \|\mathbf{x} - \mathbf{x}'\| & \text{if } \mathbf{x} \in \Omega_2 \end{cases} \tag{20}$$

This gives an implicit definition of the interface,

$$\Gamma(t) = \{\mathbf{x} \in \Omega \mid \varphi(\mathbf{x}, t) = 0\}. \tag{21}$$

The interface moves according to the flow of the fluids. This advection is performed directly with the function $\phi$, and for this reason the level-set method is referred to as an implicit interface capturing method. The advection equation is then

$$\frac{\partial \varphi}{\partial t} + \hat{\mathbf{u}} \cdot \nabla \varphi = 0, \tag{22}$$

where $\hat{\mathbf{u}}$ is the fluid velocity field at the interface, extrapolated to the whole domain (as suggested by Adalsteinsson and Sethian [92]), which can be found by solving

$$\frac{\partial \hat{\mathbf{u}}}{\partial \tau} + S(\varphi)\mathbf{n} \cdot \nabla \hat{\mathbf{u}} = 0, \quad \hat{\mathbf{u}}|_{\tau=0} = u, \tag{23}$$

Here $\tau$ is a pseudo time, and $S$ is a smeared sign function which is zero at the interface, $S(\varphi) = \varphi/\sqrt{\varphi^2 + 2\Delta^2}$. We assume here that the Eulerian grid spacings are equal and denote these by $\Delta_x = \Delta_y = \Delta$. This equation is in principle solved to steady state, i.e. $\tau \to \infty$. In a recent paper, Sabelnikov et al. [93] presented an alternative approach which appears promising, since it has a lower computational cost.

As the level-set field is advected by Equation (22) it will become distorted and lose its signed distance-property. Because of this, the level-set function is reinitialised at regular intervals by solving

$$\frac{\partial \varphi}{\partial \tau} + S(\varphi_0)(|\nabla \varphi| - 1) = 0, \tag{24}$$

$$\varphi(\mathbf{x}, 0) = \varphi_0(\mathbf{x}), \tag{25}$$

to steady state [94, (7.4)]. Even though Equation (23) and Equation (24) are defined for the whole domain, we are only interested in the extrapolated velocity and the reinitialised field in a neighbourhood around the interface.

Interestingly the characteristics of both Equation (22), Equation (23) and Equation (24) originate at the interface and point outwards. This implies that if one solves the equations not for $\tau \to \infty$, but rather for $\tau \to N\Delta$, $N$ e.g. equal to 3, it gives a level-set function which is correct in a narrow band of width $3\Delta$ around the interface. This significantly reduces the computational cost of the method; see e.g. [92] for further details.

The properties required to calculate forces coming from a fluid interface are the interface normal vectors and curvature. Both of these are computed directly from $\varphi$,

$$\mathbf{n} = \frac{\nabla \varphi}{|\nabla \varphi|}, \quad \kappa = \nabla \cdot \mathbf{n}. \tag{26}$$

*2.4.2. The ghost-fluid method*

Given an interface-capturing method such as the level-set method, yet another method is required to impose the difference in material properties and the interfacial tension. Different methods are available, and one distinguishes between sharp-interface and smeared-interface methods. A sharp-interface method (such as the ghost-fluid [95] or immersed-interface methods [96]) is more accurate, but also more difficult to implement, as compared to a smeared-interface method (such as the continuum-surface-force [97] or immersed-boundary [98] methods).

With a smeared-out method, a mollified delta-function is used to spread a singular force out to several grid cells. With such an approach, the normal finite-difference approximations to derivatives can be used as there are no discontinuities in the solution, but rather very steep, smooth transitions.

By contrast, with the ghost-fluid method as used in this work, the discontinuities are incorporated directly into the numerical stencils. This means that there is an actual jump in the solution, and jump conditions are used to relate the values across the interface. For the case of two-phase flow with a constant interfacial tension, the jumps are given by

$$[\![\mathbf{u}]\!] = 0, \tag{27}$$

$$[\![p]\!] = 2[\![\mu]\!]\mathbf{n} \cdot \boldsymbol{\nabla}\mathbf{u} \cdot \mathbf{n} - \gamma\kappa, \tag{28}$$

$$\begin{aligned}[\![\mu \boldsymbol{\nabla}\mathbf{u}]\!] = [\![\mu]\!]\Big( &(\mathbf{n} \cdot \boldsymbol{\nabla}\mathbf{u} \cdot \mathbf{n})\mathbf{n}\mathbf{n} + (\mathbf{n} \cdot \boldsymbol{\nabla}\mathbf{u} \cdot \mathbf{t})\mathbf{n}\mathbf{t} \\ &- (\mathbf{n} \cdot \boldsymbol{\nabla}\mathbf{u} \cdot \mathbf{t})\mathbf{t}\mathbf{n} + (\mathbf{t} \cdot \boldsymbol{\nabla}\mathbf{u} \cdot \mathbf{t})\mathbf{t}\mathbf{t}\Big)\end{aligned} \tag{29}$$

Here $\mathbf{n}, \mathbf{t}$ are the normal and tangent vectors at the interface, and we denote tensors formed by the outer product as e.g. $\boldsymbol{\nabla}\mathbf{u}$. We take the normal vector to be pointing outwards on a drop, and then the jump

$[\![\cdot]\!]$ is the difference between the external and internal values, e.g. $[\![\mu]\!] = \mu_2 - \mu_1$. It should be noted that these expressions have been written in a form that gives faster code when implemented, see Lervåg [99] for a derivation and for a more thorough description of the ghost-fluid method.

In the hybrid method developed here, these equations are used without the term $\gamma\kappa$ in Equation (28), since the tension is then handled by the immersed-boundary method instead. The term is included when the regular level-set/ghost-fluid method is used as a reference for testing the hybrid method.

*2.4.3. Motivation for the hybrid method*

To compute the tensions using Equations (17) and (18) requires knowledge of the interfacial deformations $\lambda_s, \lambda_\phi$. We may prove that the level-set function, or any similar scalar marker function, does not contain the information required to compute this. Equivalently, the marker function does not contain information about compression or stretching of the interface. To have compression or stretching of an interface in incompressible flow, assuming no sources or sinks are present, the velocity component tangential to the interface has to be nonzero. By considering the projection operator

$$P_{\parallel}(\varphi) = (1 - \nabla\varphi(\nabla\varphi\cdot\,))$$

which projects $\mathbf{u}$ into the space of velocity fields that are tangential to the interface, one may easily prove, using the signed distance property of $\varphi$, that only the velocity component normal to the interface gives a non-zero contribution in the advection equation. In other words, the interface representation $\phi$ is invariant under velocity fields tangential to the interface. To store information about interfacial compression or stretching in an interface capturing method which uses an Eulerian marker function, one must resort to additional data structures to represent interfacial strain.

Alternatively, we may consider a hybrid interface-tracking method. Such methods have been successful at combining the best features of several methods, e.g. in the coupled level-set/volume-of-fluid (CLSVOF) method [100]. In the present work we have developed a hybrid level-set/ghost-fluid/immersed-boundary method. The immersed boundary method provides not only the required information about compression and stretching, but is also widely used and thoroughly tested with a general tension (i.e. elasticity and interfacial tension). Originally developed for simulating biological systems, e.g. blood flow through a heart [98], the immersed boundary method has been successfully applied to the simulation of red blood cells [12], which have similar properties to drops covered with elastic membranes.

Another important motivation for using the immersed boundary method is that it allows for refining the discretisation of the interface independently of the Eulerian grid. This increases the accuracy of the interfacial representation while the Eulerian grid remains the same, as indicated by the results of standard interface-capturing method test cases in Section 4.1. In particular for the crumpling drop case of interest here, this represents a large saving of computational cost, since crumpled interfaces like those discussed in Section 5, represented using the level-set function, would require at least an order of magnitude more Eulerian grid points than what is required to represent the flow field with sufficient accuracy. This would cause simulation times to be at least two orders of magnitude larger (one order of magnitude from increased cost in the Poisson solver, and one from the increased number of time steps required due to the stability condition). The simulations considered in Section 5 have runtimes of a few days running in serial; parallelisation would give some improvement in the time-to-solution, but even state-of-the-art solvers for the pressure Poisson equation show limited performance gains when the number of unknowns per CPU core is below $O(10000)$. Thus if one was to use an extended level-set/ghost-fluid method, having data structures to represent interfacial strain, and a parallelised code, the runtime for one of these cases would be of the order of months and the effort to implement the method would be much larger.

The reason for not completely switching to the immersed-boundary method is that the handling of density and viscosity differences across the interface is less accurate than with the level-set/ghost-fluid method; with the immersed-boundary approach the contributions from the viscosity difference in the jump conditions Equations (28) and (29) are typically not taken into account (see e.g. [101]), similar to when the level-set method is used together with the continuum-surface force method [97]. The reason for retaining the level-set method is that this eases the implementation, and that it may allow for simulations of drop coalescence in an

extended version of the hybrid method, since the level-set method handles changes in the interface topology very well.

*2.4.4. The immersed boundary method*

The key point of the immersed boundary method [72] is to allow solving the Navier-Stokes equations, or other continuum equations, on an Eulerian regular grid, while handling a large class of arbitrary deformable or rigid bodies embedded in the same domain. These bodies are described by Lagrangian coordinates. Thus a key element of the method is the transformations between the Lagrangian and Eulerian coordinates, and vice versa.

In addition to flexible interfaces as considered here, the immersed-boundary method can be used to simulate rigid bodies. This has been widely employed for simulations in complex domains. With this approach, the equations become very stiff, and thus the implicit forcing method has been constructed [102]. For the case of interest here, namely flexible interfaces, the explicit forcing method as used in the original immersed-boundary method is sufficient. Even with an explicit time integration scheme, the method is stable given that the time step is sufficiently small [103].

When using the immersed-boundary method to implement a generalised interfacial tension, we follow the procedure given in [104]. The interface is imagined as a continuum of elastic fibres immersed in the fluid. These fibres serve as a device for deriving the model. They do not have a mass nor do they occupy a volume, but together with the fluid they are immersed in, they act as a viscoelastic material. The fibres are arranged in a mesh parametrised by three space coordinates, which we take to be $(\phi, r, s)$ with reference to Figure 3. With this framework, fixing two of the space coordinates, e.g. $(\phi, r)$, uniquely determines a fibre. The last coordinate, $s$, is then a parametrisation along the elastic fibre given by the fixed values of $(\phi, r)$.

For the case of interest here, namely a drop interface that has no thickness, one coordinate is given by the other two, i.e. $r = r(\phi, s)$; for a spherical drop $r$ would be constant. Moreover, we consider the axisymmetric case, meaning that $r = r(s)$ and that nothing depends on $\phi$. This means we consider the situation illustrated in Figure 3, i.e. a single fibre going in the meridional (or $s$) direction of the drop, which is discretised by many points. For each such point there is also a fibre going in the azimuthal direction, which is not discretised.

Using Peskin's notation, we write the strains as e.g. $\lambda_s = |\frac{\partial \mathbf{X}}{\partial s}|$. We then have [104] the forces from the interface acting on the fluid given as

$$\mathbf{f} = \frac{\partial T_s}{\partial s}\mathbf{t} + T_s \left|\frac{\partial \mathbf{X}}{\partial s}\right| \kappa_s \mathbf{n} + T_\phi \left|\frac{\partial \mathbf{X}}{\partial \phi}\right| \kappa_\phi \mathbf{n}. \tag{30}$$

From this we see that the force consists of a component along the fibre in the direction $\mathbf{t}$, as well as a component in the principal normal direction, pointing towards the centre of the osculating circle of the curve, $\mathbf{n}$. As previously noted, there is no force in the binormal direction, $\mathbf{t} \times \mathbf{n}$.

If we assume no elasticity and a constant interfacial tension, $T_s = T_\phi = \gamma$, Equation (30) becomes

$$\mathbf{f} = \gamma \left( \left|\frac{\partial \mathbf{X}}{\partial s}\right| \kappa_s + \left|\frac{\partial \mathbf{X}}{\partial \phi}\right| \kappa_\phi \right) \mathbf{n} \tag{31}$$

and the tangential force disappears. This corresponds to the normal two-phase flow situation with a simple interface described only by interfacial tension, and will serve as a test case for the hybrid method. The deformations entering into this expression serve as normalisation factors, since the original expressions are derived with reference to the undeformed coordinate system. This point may be confusing at first; the reader is referred to the thorough derivation in [104]. The parenthesis in this expression corresponds to the mean curvature of the drop, so the entire expression corresponds to the familiar Laplace-Young formula.

To implement the tensions numerically requires computing the interfacial deformations. Let

$$\|\mathbf{X}\|_i^k = \|\mathbf{X}_k - \mathbf{X}_i\| \tag{32}$$

be the Euclidean distance between Lagrangian points $i$ and $k$. For simplicity we restrict the disposition here to the fully two-dimensional case, where $T_\phi = 0$ and the tension $T$ is given as

$$T_s = K_a \left( \left| \frac{\partial \mathbf{X}}{\partial s} \right| - 1 \right) + \gamma \tag{33}$$

Discretising this equation gives the following expression for the tension at point $i$, $T_{s,i}$:

$$T_{s,i} = K_a \left( \frac{\|\mathbf{X}\|_i^{i+1} + \|\mathbf{X}\|_{i-1}^{i}}{l_i + l_{i-1}} - 1 \right) + \gamma, \tag{34}$$

where $l_i$ is the equilibrium length between point $\mathbf{X}_i$ and $\mathbf{X}_{i+1}$. This gives the tension for each Lagrangian point along the boundary, which is then used in a discretised version of Equation (30),

$$\mathbf{f}_i = \frac{T_{s,i+1} - T_{s,i-1}}{2} \mathbf{t}_i + T_{s,i} \frac{\|\mathbf{X}\|_i^{i+1} + \|\mathbf{X}\|_{i-1}^{i}}{2} \kappa \mathbf{n} \tag{35}$$

to compute the discretised interfacial force. This force enters the right-hand side of the discretised Navier-Stokes equations on the Eulerian grid points close to the interface. The force is smeared out to these points using the mollified delta function, which is made up of combinations of one-dimensional mollified delta functions $\delta(r)$.

In contrast to other smeared-interface methods, the delta function in the immersed-boundary method is uniquely determined by six requirements on the properties of this function. The reader is referred to [72, sec. 6], [104], as well as the previously mentioned MSc thesis by Lysgaard [90], for details of the delta function construction, as well as description of the spreading of Lagrangian quantities to the Eulerian grid, and the interpolation in the opposite direction. The resulting one-dimensional delta function, which is the basis for both the interpolation and spreading operations, is

$$\delta(r) = \begin{cases} \frac{1}{8} \left( 3 - 2|r| + \sqrt{1 + 4|r| - 4r^2} \right), & |r| \leq 1 \\ \frac{1}{8} \left( 5 - 2|r| - \sqrt{-7 + 12|r| - 4r^2} \right), & 1 \leq |r| \leq 2 \\ 0, & 2 \leq |r| \end{cases} \tag{36}$$

where $r$ is the distance e.g. from a Lagrangian point to the Eulerian grid cell centre.

We remark that if the distance between two Lagrangian points is too big, the spreading operations using the delta function will not approximate the continuous versions correctly. For this reason it is required that two Lagrangian points never be further apart than half the width of an Eulerian grid cell.

In the proposed method, cubic splines are used to generate a smooth analytic parametrisation of the interface. The main advantage of this is that properties such as the curvature, tangent- and normal vectors are all naturally defined for a cubic spline. Figure 4 shows the immersed boundary elements around the point with index $i$ together with their different properties, and where they are defined. The cubic spline fitted to the points is only evaluated at the nodes. Because of this the curvature is only available at these points. The same applies to the normal vectors, which are directly calculated from the first derivative of the spline at the nodes. On the other hand, line segments are computed as the difference in position between two adjacent points. This means that lengths are defined on the segments, and not on the nodes. Note that the cubic spline going through the points is not shown in this figure, but it is used to compute the curvature $\kappa$ and the normal vector $\mathbf{n}$.

It should also be noted that the differences in segment length are exaggerated in Figure 4, since the tangential term in the interfacial force will very quickly eliminate such differences. This is in line with what one expects from such longitudinal waves, which are known from theory [105] and experiments [106] to be extremely rapid. This can also be understood intuitively since, in contrast to a regular capillary wave, a longitudinal surface wave displaces essentially no mass, and thus inertial effects are very small.

When computing the interfacial force on each node, all variables are required at the node. As mentioned, the segment-lengths are not stored at the nodes. An option would be to use the cubic spline to calculate the

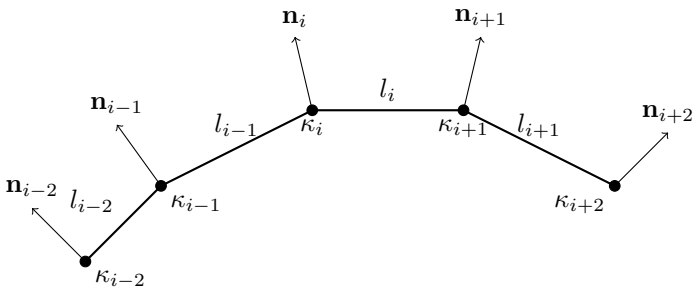


Figure 4: Part of immersed boundary grid showing where different values are located.

length, but this requires the numerical evaluation as well as inversion of an elliptic integral. To keep the method simple, we approximate the segment length as the average of the linear distance from the node in question to its two neighbours. The curvature and unit normal vectors remain analytically evaluated from the cubic spline.

In total, this approach encapsulates all the surface effects we need to simulate in one coherent framework. If, say, the elasticity of the material is a function of temperature, or the elasticity is found to be non-Hookean, or some relaxation behaviour is observed that makes the elastic modulus a function of the applied strain, these effects can easily be accounted for by modifying Equation (33).

*2.4.5. Computing the level-set function from the immersed boundary*

When using both the immersed boundary method and the ghost-fluid method to calculate interface forces, special care has to be taken to make the methods consistent. The following technique is proposed for that. The geometry is completely determined by the Lagrangian points along the interface. In each stage of the time integration method, the shortest distance from the Eulerian points to the Lagrangian boundary is computed. In other words, we compute the level-set function purely from the immersed boundary.

This has several advantages. First, advection is moved from the level-set function to the immersed boundary. When no advection of the level-set function is required, it is no longer needed to reinitialise it, Equation (24), or extrapolate the velocity, Equation (23). These routines are somewhat costly, and their saving leads to a $\sim 25\%$ reduction in wall clock run time for some typical two-phase simulations. Second, using this approach, the level-set function is always the best possible approximation to the exact signed distance function for the given Eulerian grid. Third, given equal initial conditions for the immersed boundary and the level-set field, the two descriptions of the interface may not be consistent with respect to each other, meaning that after some time, $t$, the advection of the level-set function and the Lagrangian points could cause the two methods to have slightly different locations for the interface [2]. This is problematic because the interfacial forces would appear at two different interfaces rather than one. This inconsistency disappears when reinitialising the level-set function from the immersed boundary at every timestep.

The algorithm for computing the level-set function from the Lagrangian points is as follows.

↪ Loop over the Lagrangian points representing the interface

- ↪ For each line segment connecting two points, compute its bounding box.
- ↪ Grow the bounding box such that it contains the widest Eulerian stencil used in the discretised reinitialisation equation.
- ↪ Loop over the Eulerian grid points inside the bounding box

[2]The reason for this is that the immersed boundary points can have sub grid details. This means that inside a grid cell there will be differences between the level set and the immersed boundary. Over time these will grow bigger than one grid cell because of advection. At that point, the two interface descriptions are not consistent with each other.

↪ Compute the shortest distance from this grid point to the line segment using standard formulae.

↪ Compute whether the grid point is inside or outside of the closed interface using a standard point-inside-polyhedron algorithm.

↪ From these two results, compute the signed distance.

↪ If this is the smallest distance computed for this grid point so far in the outer loop, store it as the signed distance for this grid point.

*2.4.6. Penalisation method*

As will be seen in Section 5.2, we want to be able to simulate solid objects in our domain, in addition to the two-phase flow with complex interfaces. To achieve this we utilise a standard $L_2$ penalisation method [107] since it is very easy to implement (literally just twenty lines of code) and since it can also be used to enforce a flow field such as the desired suction inside a pipette. With the penalisation method, the flow field exists inside the solid objects, but is forced to be approximately equal to zero, or in general equal to a specified field $\mathbf{u}_{\text{spec}}$, through a forcing parameter $1/\eta$ which enters in an additional term $(1/\eta)\chi(\mathbf{u}_{\text{spec}} - \mathbf{u})$ added to the right-hand side of the momentum equation. Here the scalar field $\chi$ is a marker function for the solid body, so it is 1 inside the body and 0 outside it. One can think of the penalisation term as an additional body force which outside the body is zero and inside the body is proportional to the difference between the actual and the prescribed flow field. In [107] proofs of the existence and uniqueness of solutions with this method, as well as an error estimate, are given. The error is of the order of $\eta$. To get good results, one would naively set $\eta = 0$ and get zero error, but as the time step needed for stability is proportional to $\eta$ there is the usual trade-off between speed and accuracy.

*2.4.7. The time step restrictions*

In the simulations, the appropriate time step is adjusted dynamically using the conditions given here, in order to have time steps as large as possible without causing the method to become unstable. Following [108, sec 3.8], we take the contribution from the advection term into account with

$$\mathrm{M}_c = \frac{\max u_x + \max u_y}{\Delta}, \tag{37}$$

where $\Delta$ is the width of an Eulerian cell and $\max u_x, \max u_y$ are the largest magnitudes taken by the velocity components in the simulation domain. The contribution of the viscous stress to the time step restriction is taken into account with

$$\mathrm{M}_v = \max\left(\frac{\mu_1}{\rho_1}, \frac{\mu_2}{\rho_2}\right)\frac{4}{\Delta^2}. \tag{38}$$

These are combined with the contribution from the interfacial force $\mathbf{f} = [f_x \ f_y]^T$ to form the time step restriction

$$\frac{\Delta t}{2}\left((\mathrm{M}_c + \mathrm{M}_v) + \sqrt{(\mathrm{M}_c + \mathrm{M}_v)^2 + \frac{4f_x + 4f_y}{\Delta}}\right) \leq C \tag{39}$$

From smearing out the interfacial force density $\mathbf{F}$ using the mollified delta function $\delta_\Delta$, we have that $\mathbf{f} = \mathbf{F}\delta_\Delta$ and since $\delta_\Delta \leq \frac{1}{\Delta}$, cf. Equation (36), the time step restriction can be written as

$$\frac{\Delta t}{2}\left((\mathrm{M}_c + \mathrm{M}_v) + \sqrt{(\mathrm{M}_c + \mathrm{M}_v)^2 + \frac{4F_x + 4F_y}{\Delta^2}}\right) \leq C. \tag{40}$$

In this final condition, $C$ is the time step safety factor, typically $C = 0.5$. Finally, as mentioned in the previous section, when the penalisation method is used, the timestep must also fulfill $\Delta t \leq \eta$ where $\eta$ is the penalisation parameter.

## 3. Summary of the proposed method

At this point we may assemble the proposed multiscale method in its entirety.

- **At the nanoscale:** consider a tiny patch of the interface, $\sim 300$ nm$^2$:
  - A volume around this patch is simulated using coarse-grained molecular dynamics.
  - Accurate models for water, heptane, toluene and asphaltenes are used.
  - The domain is elongated normal to the interface. Large systems of $\sim 10^6$ atoms are simulated.
  - The interfacial tension $\gamma$ is computed from Equation (7).
  - Using volume-preserving deformations, the elasticity $K_a$ is computed from Equation (9).
- **At the macroscale:** two-phase flow simulation of drop with complex interfaces:
  - Flow is governed by Equations (10) and (11), solved using numerical methods described in Section 2.4.
  - The interface is handled with the new hybrid level-set/ghost-fluid/immersed-boundary method.
  - Level-set/ghost-fluid method gives a sharp handling of density and viscosity jumps using Equations (27) to (29).
  - Immersed-boundary method gives accurate interface representation, and computes the tension $T$ with Equations (17) and (18) using $\gamma$ and $K_a$ from the nanoscale.
  - The forces caused by $T$ are computed from Equation (31) and distributed from the Lagrangian points to the Eulerian grid using Equation (36).
  - The level-set function is computed from the Lagrangian points using the algorithm in Section 2.4.5.

In Figure 5 the method is summarised, showing the vectors and interface representation living on the Eulerian grid, the immersed boundary Lagrangian points and the tensions acting on them, and in the corner the molecular dynamics simulation which represents a tiny patch of the interface and is used to estimate the properties $K_a$ and $\gamma$.

We will now proceed to validate the different components that make up this method. We begin in Section 4.1 with the macroscale method, and continue in Section 4.2 with the nanoscale, where the models for different fluids and for the asphaltene molecules are considered.

## 4. Validation

We will now present validation results for both the nanoscale and the macroscale models. We first consider the hybrid macroscale method and demonstrate that this method gives the correct results on several test cases. Then we consider the nanoscale models for both the simple fluids and the more complex asphaltene molecules.

### *4.1. Macroscale: validation*

In this section we will demonstrate the validity of the developed hybrid method. We start by demonstrating the superior resolution of the immersed-boundary method over the standard level-set method, as previously mentioned. To this end we employ two standard test cases for interfacial advection, namely the drop in vortex test and Zalesak's disk test.

Following this, we consider the case of an initially elongated spheroidal drop relaxing under interfacial tension. The case is considered both for a two-dimensional and for an axisymmetric drop, and it is also considered both with and without density and viscosity differences across the interface. In summary, we demonstrate that the methods converge to the same solution under grid refinement. For further verification, see [90]. For the continuum simulations presented in this work, we provide tables with details of the configuration and parameters used in Appendix A.

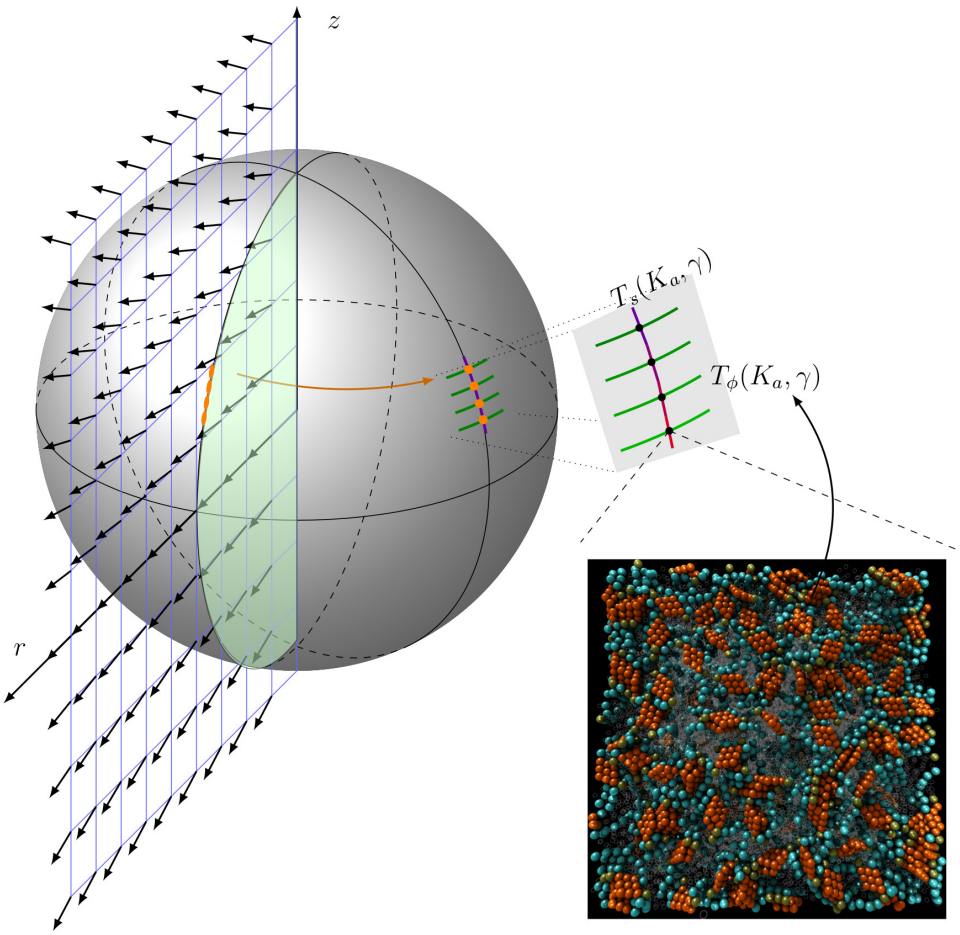


Figure 5: Illustration of the proposed method. On the Eulerian $(r, z)$ grid, the flow field $\mathbf{u}$ (vectors) and the level-set function $\phi$ representing the green-shaded portion of the droplet are shown. Some of the Lagrangian immersed-boundary points are shown in orange, with lines as before indicating the tensions $T_s$ and $T_\phi$. For a tiny patch on the interface, we compute the interfacial properties $K_a$ and $\gamma$ using molecular dynamics simulations (lower right corner). These properties are used in the calculations of the tensions. Note that the colours used in the molecular dynamics simulation snapshot do not have any relation to the other colours in the figure.

#### *4.1.1. Drop in vortex*

A standard test of advection for interface-tracking methods is the drop in a potential vortex [109]. Here a drop is placed in the unit box, and a static potential vortex advects it. The velocity field is given by

$$u_x = -2\big[\sin(\pi x - \pi/2)\big]^2 \cos(\pi y - \pi/2)\sin(\pi y - \pi/2) \tag{41}$$

$$u_y = -2\big[\cos(\pi y - \pi/2)\big]^2 \sin(\pi x - \pi/2)\cos(\pi x - \pi/2) \tag{42}$$

The remaining parameters for this test are given in Table A.1.

At some time $t = T/2$, the flow field is reversed, and the simulation is run until $t = T$. Then the initial interface is compared with the final one. Figure 6 shows the initial condition (a), the interface at half time (b) where $t = T/2 = 3.5$, and the final interface for both the level-set and the immersed boundary method, in red and black colours, respectively.

We see that the immersed boundary method has no visible mass loss, while the level-set representation loses mass when the drop gets stretched thinner than a grid cell. The reason for the large level-set mass loss

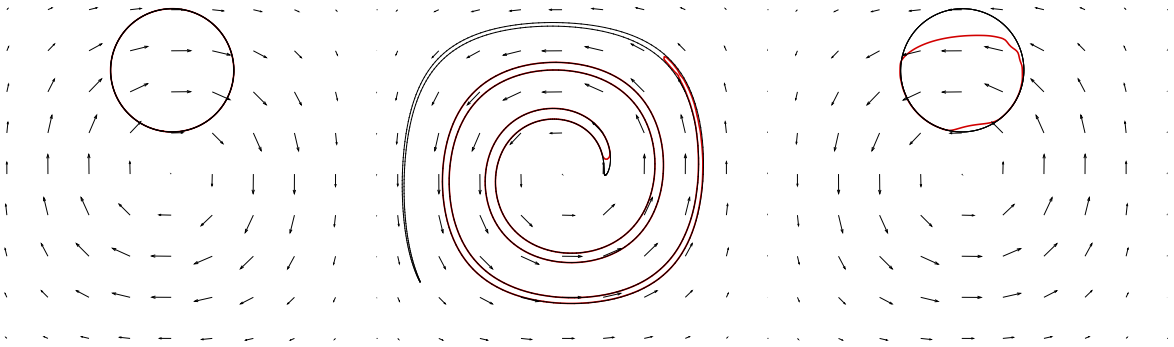

(a) $t = 0$ (b) $t = 3.5$ (c) $t = 7$

Figure 6: Drop in potential vortex. Red is level-set solution while black is the immersed boundary. Velocity vectors are shown for every 20 grid points in each direction.

is that when two interfaces come this close together, the discrete level-set function does not have the required resolution to switch sign. This follows from the Nyquist-Shannon theorem. The immersed boundary method does not have this restriction. If one wanted to represent the smaller features with level-set representation, one choice would be to double the grid resolution. For two dimensions this would make the computational cost increase quadratically. To get the same increase in resolution with the immersed boundary method, one would need to double the number of points, this would only double the amount of work needed. Thus immersed boundary scales considerably better than level-set with respect to the interface resolution.

The previous argument makes immersed boundary seem superior to level-set when it comes to resolution. However, this is not the whole story. For the immersed boundary to represent a non-smooth sub-grid feature, the Lagrangian points have to be advected in a sub-grid way. With the immersed boundary method, the Lagrangian points are advected using an interpolated of the velocity field from the Eulerian grid. This means that the highest wave number that can be created in the immersed boundary representation *by the flow* is proportional to $1/\Delta$ (where $\Delta$ is the width of the Eulerian grid cells). For smooth velocity fields, like this potential vortex, the immersed boundary method has some sub grid resolution. This is because it can accurately represent stretching, squishing and other smooth transformations that lead to sub grid details. Also, in the case of the interface crumpling as will be discussed in later sections, the immersed boundary representation will produce wrinkles inside each grid cell.

*4.1.2. Zalesak's disk*

Another interesting difference between an Eulerian and Lagrangian description of geometry is the effect of grid alignment. This effect can be seen in the next test, Zalesak's disk [110]. Here, a slotted disk is put in a velocity field that has constant angular velocity, corresponding to rigid body rotation. The boundary is advected one or several revolutions and the result is inspected. Further details of the case are given in Table A.2.

From Figure 7 it is clear that the immersed boundary resolves the rotated disk better than the level-set function. During the rotation, information is lost in the level set, while the immersed boundary is virtually not affected. The reason for this is that the level set, based on an Eulerian grid, cannot represent non-smooth features that are not aligned with the grid perfectly. This means that over the duration of the rotation, small errors in the interface position creeps in as a consequence of the interface not being straight and aligned with the grid. In the immersed boundary method, the grid has no preference about the orientation of the interface. When it comes to the drop-in-vortex test, Section 4.1.1, one may argue that the difference between the two methods is exaggerated by the specifics of the test, to the detriment of the level-set method. There does not seem to be any such argument for Zalesak's disk. The immersed boundary method is fundamentally better at preserving non-smooth features like corners without smearing. In real life, non smooth interfaces occur e.g. when two drops coalesce.

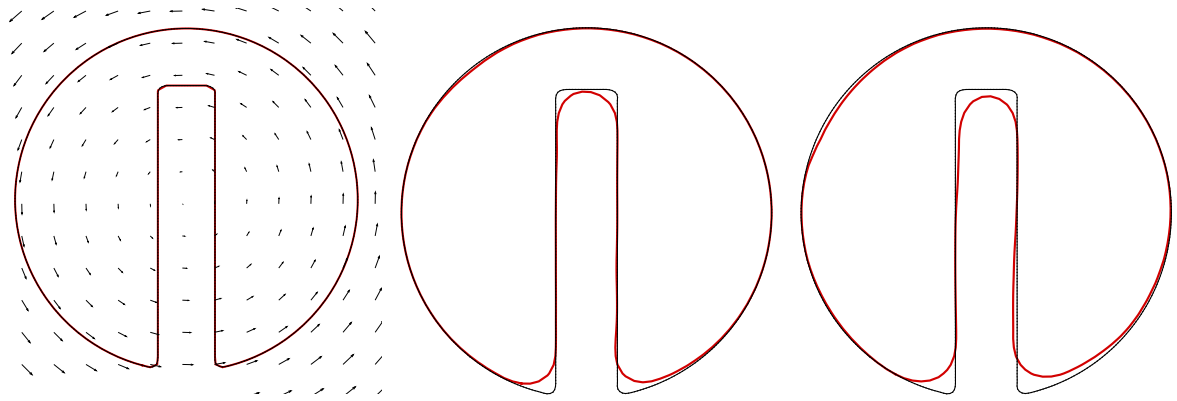

(a) $t = 0$ (b) $t = 40$ (c) $t = 80$

Figure 7: Zalesak's disk for 0, 1 and 2 revolutions. Red shows level-set interface while black shows immersed boundary. The velocity field is constant in time and corresponds to rigid body rotation.

*4.1.3. Comparison with reference method*

We have now verified that the immersed boundary method captures the interface correctly under advection. Next we need to verify that the forces from the boundary on the fluid are implemented correctly. The handling of the viscosity and density jumps must also be verified to be correctly coupled with the immersed boundary. The technique chosen for this was to compare the proposed method, Section 3, with a reference method, the level-set method with the ghost fluid method, which has previously been verified and validated [84, 85, 86, 87, 88, 89]. To have some measure of the drop dimensions during oscillations, the horizontal and vertical axis lengths are used. These parts of the drop are the ones most rapidly advected, with the highest pressure differences and curvatures. Thus any differences between the two methods would be most pronounced at these points.

In the first test, an ellipsoidal drop is relaxing to its equilibrium, a sphere, driven by interfacial tension. The purpose of this test is to verify that interfacial tension simulated with the proposed hybrid method gives the same results as when simulated with the standard level-set/ghost-fluid method. There is no gravity and no density or viscosity differences in this test. This way, all forces are generated by interfacial tension as the ellipse relaxes to equilibrium. The parameters of the test are listed in Table A.3. The test was run for increasing grid resolutions to see how the two methods compare under refinement. The result for the axisymmetric simulation can be seen in Figure 8. We see that under grid refinement, the proposed method converges to the same answer as the previously verified and validated implementation of the level-set/ghost-fluid method. This demonstrates that the hybrid level-set/ghost-fluid/immersed-boundary method gives the correct result. For corresponding tests in two dimensions, see [90].

This test shows that the proposed method converges to the same solution as the reference method for a relaxing ellipse driven by interfacial tension. For the coarsest grid, it appears the hybrid method is the least accurate. This is likely caused by the disagreement between the Eulerian and Lagrangian interface representations becoming significant when the curvature of the interface is no longer much smaller than $1/\Delta$.

This test confirms that the method is consistent, but there is no jump in density or viscosity in this case. As discussed previously the proposed method will treat density and viscosity jumps in a sharp fashion, while the tension in the interface is handled in a smeared-out fashion. To verify that this also gives consistent results, a simulation of a similar case, i.e. a relaxing ellipse driven by interfacial tension was set up. Instead of equal density and viscosity, the density ratio is now 2 and the viscosity ratio is 10. These parameters are representative for the case of a water drop in oil. The simulation was run on a moderately fine grid, $N = 400$, where good agreement was found between the two methods in the previous test. The full set of parameters for the simulation are listed in Table A.4. The simulations were run both for 2D and axisymmetric flow for both methods.

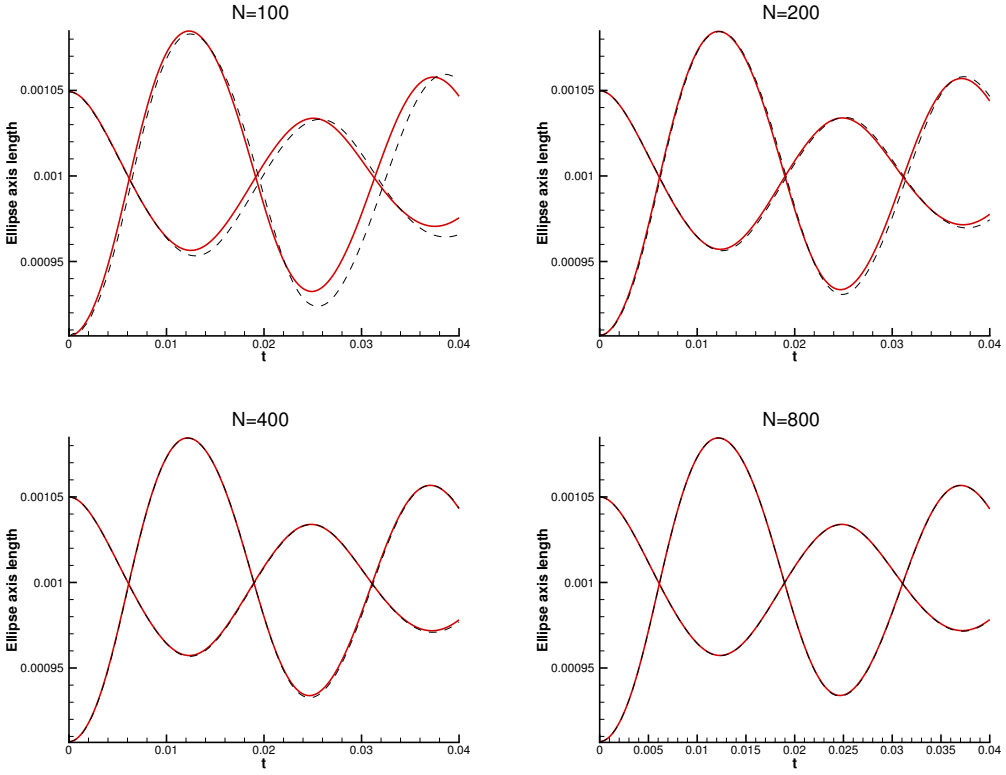


Figure 8: Drop axis lengths for the axisymmetric relaxing drop. Red is the reference solution, dashed black is immersed boundary solution. The two methods converge to the same solution as the grid is refined.

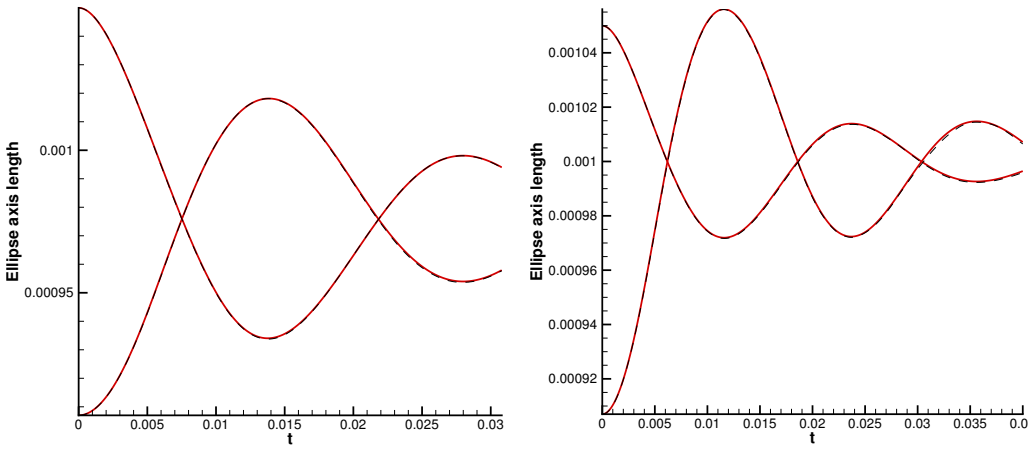


(a) Two-dimensional drop.

(b) Three-dimensional, axisymmetric drop.

Figure 9: Comparison of drop axis lengths for the reference method and proposed method with a viscosity and density jump. Red is reference method while dashed black is proposed method.

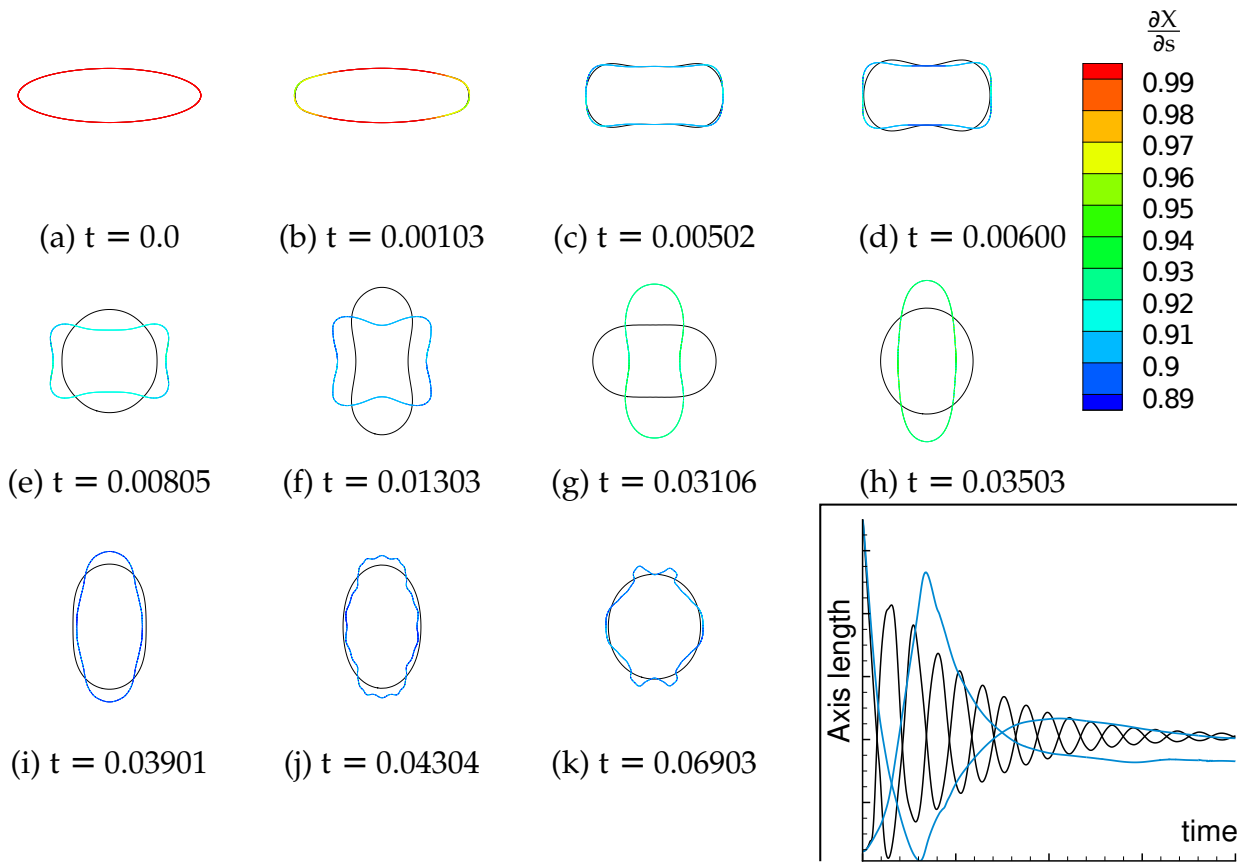


Figure 10: Several frames of the two-dimensional simulation with elastic membrane, (coloured) together with the clean interface, (black). The colours indicate the relative length of the interface compared to its equilibrium length. The inset in the lower right corner shows the time evolution of the horizontal and vertical axis of the clean (black) and the contaminated (blue) interface, which indicates that clean drop undergoes many oscillations during this time, while the contaminated drop only undergoes one.

As seen in Figure 9 the two methods are in agreement both for two-dimensional and axisymmetric flow. This shows that the proposed method correctly and consistently combines the interfacial tension from the diffuse interface, with the sharp handling of viscosity and density jumps.

*4.1.4. Relaxing drop with elastic membrane*

To test the effect of additional elasticity on the interface, the relaxing ellipse was again considered. In this two-dimensional test case, the initial condition is an ellipse with both interfacial elasticity and interfacial tension, compared to the same case with zero elasticity. The parameters for this test are listed in Table A.5. At the initial state, the deformation $\frac{\partial \mathbf{X}}{\partial s} = 1$ in Equation (33), so the elasticity does not contribute to the interfacial force. One can say that from the elastic point of view, the interface is neither stretched nor compressed, but there remains the constant interfacial tension which produces a force. In this particular case, $K_a$ is set to be ten times larger than $\gamma$, which means that $T$ computed from Equation (33) will be close to zero when $\frac{\partial \mathbf{X}}{\partial s} \approx 0.9$. In other words, when the membrane is compressed to 90% of its original length, elastic forces and interfacial tension forces will be in balance.

The interface starts in the initial state shown in red in Figure 10 (a). Because of its eccentricity, interfacial tension is relatively strong on the left and right sides of the drop and it is quickly compressed, Figure 10 (b). After $5 \times 10^{-3}$ s the drop is compressed to approximately 90% of the initial length Figure 10 (c). This means that the interface no longer introduces any force, and without any viscosity or density differences the simulation would proceed as if it was momentarily single phase. As there is a significant flow still present

in Figure 10 (c), advection of the interface continues. Some of the kinetic energy which is not dissipated by viscosity goes into deforming and again stretching the interface. At $t = 3.5 \times 10^{-2}$ s, Figure 10 (h), the interface is stretched to the next maximum again, and the velocities are close to zero. Now there is not enough potential energy in the membrane to do another oscillation, it is in some sense overdamped. The interface contracts creating a crumpled drop as seen in Figure 10 (i) to Figure 10 (k). As this has happened the drop with a clean interface, in black, has oscillated towards its equilibrium shape, a circle, by going through about eight oscillation cycles.

It is clear that for these parameters, the elastic membrane has a significant effect on the time evolution of the drop, fundamentally changing its response. For clean fluids, the equilibrium interface is always the one that has the minimal interface area. The interfacial elasticity changes this situation, and the equilibrium state is no longer obvious given the initial conditions. One insight from this simulation is that for a clean drop without an elastic membrane, there exists a unique spherical equilibrium state, only given by the initial volume of the drop. On the other hand, for the drop with an elastic membrane, the equilibrium is not just a function of the initial volume, but also of the initial shape. This is because the initial shape affects what parts of the drop are stretched and compressed, which has a significant impact on the final steady state. This demonstrates that the evolution of a drop with an elastic membrane is more complex than one without.

### *4.2. Nanoscale: validation*

When running simulations of a complex multi-component system, the first thing to consider is each of the two-component systems. For the toluene-water and heptane-water systems, there is one free parameter, the binary interaction parameter $k_{ij}$, to tune in each case. There is also an important value to tune this against, namely the interfacial tension measured in experiments. For the alkane-water system with the models used here, Lobanova et al. [111] obtained the value of $k_{ij} = 0.3205$, transferable across the alkanes with different lengths. The water [44] and alkane [111] models used have been published previously. The model for toluene used here has not been published previously; see Appendix B for force field parameters for this model.

For the toluene-water system, such tuning has not been done previously, so it is done here. The system consisted of 10 000 toluene molecules and 40 000 water molecules, placed in an elongated box, and simulated at 20°C and 1 bar. After obtaining the desired temperature and pressure by simulating in the $NpT$ ensemble, the system was allowed to phase-separate such that two slabs of liquid were formed. Subsequently, the system was simulated in the $NVT$ ensemble for 50 nanoseconds to obtain the interfacial tension.

The three values for the cross-interaction parameter, $k_{ij} = (0.1, 0.2, 0.3)$, were initially tested, and subsequent guesses were refined until the value $k_{ij} = 0.241$ was found, which gave an interfacial tension in very good agreement with the experimental value of 37 mN/m [112] at this temperature and pressure. See Figure 11, where the cumulative average of the interfacial tension computed from Equation (7) is plotted as a function of the simulation time. Also plotted is the experimental result (dashed orange line) and the running average over 1000 values of the interfacial tension (blue dots).

Having the cross-interactions for the two binary systems established, verifying that the interfacial tension for the heptane-toluene or "heptol" mixture against water agrees with experiments is a good demonstration of the predictive power of the method. When discussing a heptol mixture, one must distinguish between molar ratios, convenient in simulations, and volume ratios, convenient in experiments. To avoid confusion, we will refer here to volume ratios using the notation $N : M$, and molar ratios using the notation $n/m$. The molar mass of heptane and toluene are 100.2 and 92.1 g/mol, respectively, and their densities are 684 kg/m$^3$ and 867 kg/m$^3$, respectively. This means that a 50/50 molar ratio gives a volume ratio of 1.38:1, and conversely, a 1:1 volume ratio gives a 42/58 molar ratio.

To test the prediction of interfacial tension of the heptol-water system, a corresponding simulation was set up with a 1:1 heptol mixture against water at 20°C and 1 bar. Experimental data for this interfacial tension is not available, but an accurate estimate of it can be obtained following Yarranton and Masliyah

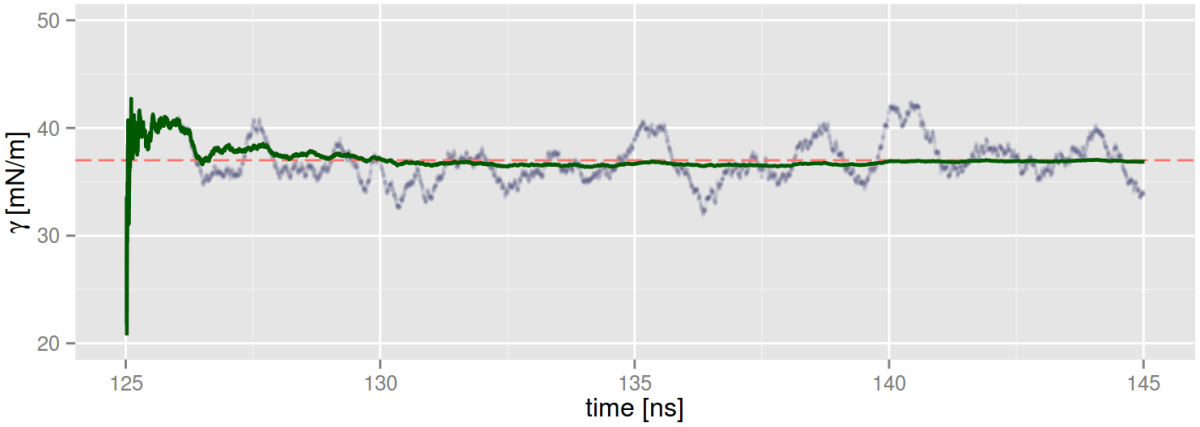


Figure 11: Interfacial tension of toluene and water, using the cross-interaction parameter $k_{ij} = 0.241$. The green line shows the cumulative average, the blue dots show the running average over 1000 points, and the dashed orange line shows the experimental value.

[113]. This procedure gives the interfacial tension of an organic mixture against water as

$$\gamma_{\text{mix}} = \gamma_2 - R_u\, T\, \Gamma_m \ln\left(1 + x_1(\exp\left(\frac{\gamma_2 - \gamma_1}{R\, T \Gamma_m}\right) - 1)\right) \tag{43}$$

where $\gamma_1$ and $\gamma_2$ are the two pure-component interfacial tensions against water, $R_u$ is the universal gas constant, $T$ is the temperature in Kelvin, $x_1$ is the molar fraction of component 1 in the mixture. We denote here toluene as component 1 and heptane as component 2. The interfacial tensions are $\gamma_1 = 37$ mN/m [112] and $\gamma_2 = 51.2$ mN/m [114]. The parameter $\Gamma_m$ is estimated as $\Gamma_m = 0.00415$ mmol/m$^2$ by Yarranton and Masliyah [113], which is shown to give good results for a wide range of alkane-aromatic mixtures. With these expressions, the interfacial tension of the mixture is computed as $\gamma_{\text{mix}} = 41.9$ mN/m.

The simulation result is plotted in Figure 12, together with $\gamma_1$, $\gamma_2$ and $\gamma_{\text{mix}}$. The simulation result matches very well the value computed from Equation (43). Note that the cross-interaction between heptane and toluene has not been tuned at all. This illustrates the predictive power of the SAFT-$\gamma$ Mie approach, i.e. that one can compute, with good accuracy, physical properties that have not been used when constructing the model.

With the simple fluids taken into account, we may proceed to consider the models for the asphaltenes. As discussed in the introduction, asphaltenes are immensely complex mixtures of different molecules that together form a solubility class. It is likely that an asphaltene molecule in solution never interacts with an identical molecule, and thus modelling the asphaltenes as a single molecule is a significant simplification. It is likely that improved asphaltene models must take the polydispersity explicitly into account, i.e. having many different types of model asphaltenes in the same simulation. This may be considered in future work.

Molecular dynamics simulations of asphaltenes in the bulk have been considered in several previous works, see e.g. refs. [115, 116, 117, 118, 119, 120, 121, 122, 123]. In these studies, the association and aggregation of asphaltenes have received particular focus, as this behaviour is very important for asphaltene deposition in rocks and in pipelines. Of particular note is the work by Boek et al. [120], where the technique of quantitative molecular representation (QMR) is used to compile a set of model asphaltene molecules, based on several experimental sources of information such as mass spectrometry, NMR, X-ray and neutron scattering studies. These model asphaltenes are employed by several subsequent authors, and have influenced the construction of the coarse-grained model asphaltenes used in this work. Sedghi et al. [122] studied the effect of different side groups and substitutions on one of these representative asphaltene molecules, and found that small changes to the chemical composition caused large variations in the aggregation behaviour.

Only very recently have molecular dynamics simulations been applied to the study of asphaltenes at the

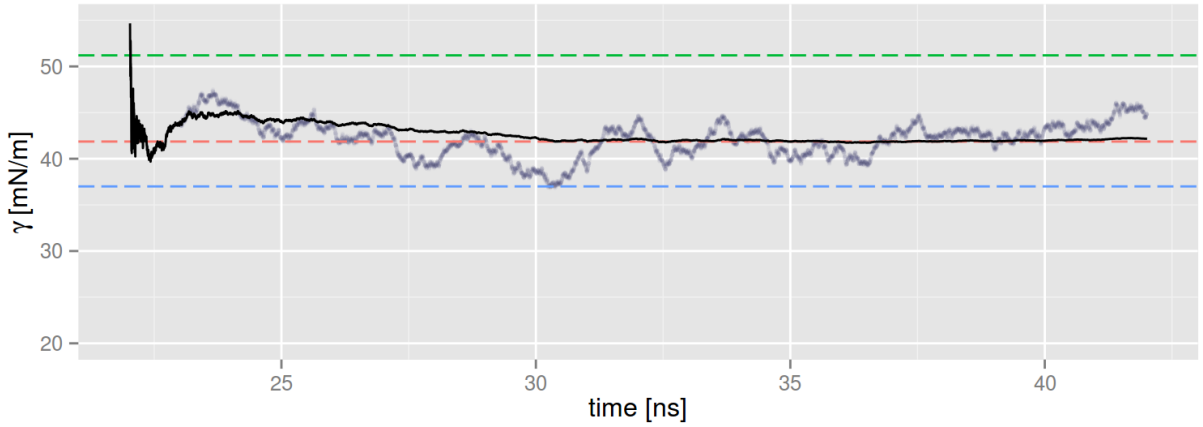


Figure 12: The interfacial tension for a 1:1 heptol mixture against water, computed from molecular dynamics simulation. Black line: cumulative average of the interfacial tension. Blue dots: running average of the interfacial tension over 1000 samples. Orange dashed line: $\gamma_{\text{mix}}$ predicted from Equation (43). Blue dashed line: interfacial tension of toluene-water. Green dashed line: interfacial tension of heptane-water.

oil/water interface. Mikami et al. [124], Liu et al. [125], as well as Yang et al. [126] used atomistically-detailed simulations to study this system. In [124, 125], the previously mentioned QMR-based model asphaltenes were employed, whereas in [126], two different model asphaltenes were proposed based on experimental measurements and used in simulations. These studies highlight the significant challenge encountered when using an atomistically-detailed approach: one is either confined to very few asphaltene molecules [126] or very short timescales [124, 125] due to the high computational cost. A coarse-grained approach, such as that used here, can provide a solution to this; see e.g. the review by Brini et al. [38] for an overview of the advantages of coarse-grained simulation for soft matter systems in general. Recent work by Ruiz-Morales and Mullins [127] employed a coarse-grained (dissipative particle dynamics) approach, but this study is also limited to considering few molecules and short time scales. Finally, it should be noted that in all these studies, the asphaltenes are initially placed at the interface.

In contrast to these limitations of either few molecules or short time scales, and enforced interfacial adsorption, we consider here simulations with up to two orders of magnitude more asphaltene molecules than considered in [126] in conjunction with two orders of magnitude longer simulation times than considered in [125]. Also the asphaltenes are not initially placed at the interface, but randomly distributed throughout the oil phase. Thus the interfacial activity is an inherent property of the model asphaltenes used here.

With this in mind, we briefly discuss the three different asphaltene models that were used in the present work. All these models are of the continental asphaltene type, i.e. they have a central core made up of aromatic rings, to which aliphatic tails are attached. The first model asphaltene, presented by Müller et al. [49], was used in the initial studies; we will refer to this as the APCH asphaltene. It is based on using anthracene beads for the aromatic core, which also contains a pyridine ring, and three tails each made from dodecane. The model behaves reasonably like an asphaltene. Results obtained with this model are discussed in Section 5.1.1.

If anything, the APCH model appears slightly too self-associative. This, together with the some advances in the SAFT-$\gamma$ Mie theory for aromatic compounds, led to the second flavor, developed partly in this work. The main difference with the first flavor is that the aromatic beads, which make up most of the core, are obtained using a version of the SAFT-$\gamma$ Mie approach that is tailored for ring-shaped molecules, as opposed to the standard version which assumes they are linearly shaped. The structure is otherwise very similar to the APCH model asphaltene. The parameters for the aromatic core beads are given in Appendix B.

Two different architectures were considered for this new flavor of asphaltenes, built from the same coarse-grained beads, but with different shapes for the aromatic core. Both have three aliphatic tails made from

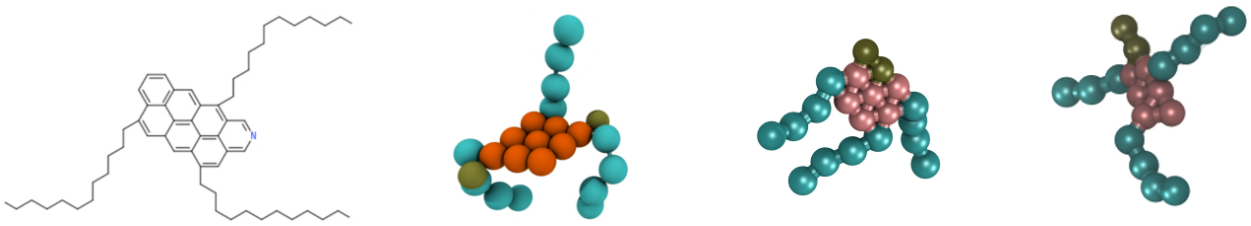

Figure 13: From left to right: corresponding chemical structure, the APCH model, the APCE model and the APCL model. Blue/green beads indicate the aliphatic tails, orange/red beads indicate the aromatic rings forming most of the core, and the tan/gold beads indicate the pyridine.

dodecane, and cores made from six beads representing six hexagonal aromatic rings, together with two beads representing a pyridine, i.e. a hexagonal aromatic ring with a single nitrogen substitution. The difference lies in that "APCE" has a more circular core, while "APCL" has a more elongated core. See Figure 13 for a comparison of the three different model asphaltenes considered in this work.

As mentioned in the introduction, the only usable definition of asphaltenes is that they are insoluble in heptane and soluble in toluene. Accordingly, it should be verified that the new model asphaltene molecules behave in this way. To test this, simulations were run with 240 asphaltene molecules in a system with 40 000 solvent molecules (heptane or toluene) at 20°C and 1 bar.

These simulations gave some interesting results which demonstrate how delicate the energy balance is in systems containing asphaltenes. The two models APCE and APCL appear very similar; however, their solubilities in heptane are completely different, as illustrated in Figure 14 which shows the behaviour in heptane. In this figure, the solvent and the aliphatic tails are omitted for clarity, so one can easily see the stacking of aromatic rings where the molecules cluster. It is readily apparent that the circular core asphaltenes cluster in heptane, while elongated core ones are soluble in heptane. It is also seen that the circular-core asphaltenes cluster with a distribution of a few large clusters, many small clusters, and some monomers; in particular, the asphaltenes do not all gather in one big cluster. This is in agreement with results from experiments (e.g. [128, 129, 130]) and atomistic simulations [119]; and it is in general agreement with the accepted Yen-Mullins model of asphaltene behaviour [131].

The APCE model thus passes the first hurdle, being insoluble in heptane. Simulations of this model in toluene also showed the correct behaviour, as illustrated in Figure 15 where the system is compared in heptane (red) and in toluene (blue) after 50 ns of equilibration. In toluene, some pairs of asphaltenes occasionally come in contact, but inspection of the trajectories showed that these pairs only stay together for about one nanosecond before they break apart again, and thus no larger clusters have time to form.

To summarise, the APCE model asphaltene fits the definition of an asphaltene molecule, forming clusters in heptane but staying in solution in toluene. In heptane, clusters of up to four molecules form after 50 ns. It is likely that five- or six-molecule clusters may form after even longer times or at higher concentrations. A closeup of a four-molecule cluster is shown in Figure 16.

## 5. Results

### *5.1. Molecular dynamics simulations of asphaltenes in oil/water systems*

The crude oil/water system has a very large (and not fully understood) parameter space, so we restrict our attention here to only a few simplified cases. The parameters that can be varied include temperature, pressure, the mixture of alkanes and of aromatics for the fluid components, the ratio between alkanes and aromatics in the fluid components, the amount of resins, the amount of asphaltenes, etc. The liquid components of a crude oil contain a range of alkanes that may extend all the way from methane (liquid at high pressure) to alkanes with 20-30 carbon atoms (liquid at high temperature). Effective models for these mixtures can be obtained by taking a true boiling point curve and dividing it into classes of pseudo-components, e.g. a mixture of $C_5H_{12}$, $C_{10}H_{22}$, $C_{15}H_{32}$, $C_{20}H_{42}$. The very simplest version of this, which we adopt here, is to use just one alkane, for which heptane is a common choice. Similarly, for the aromatic liquids there is a

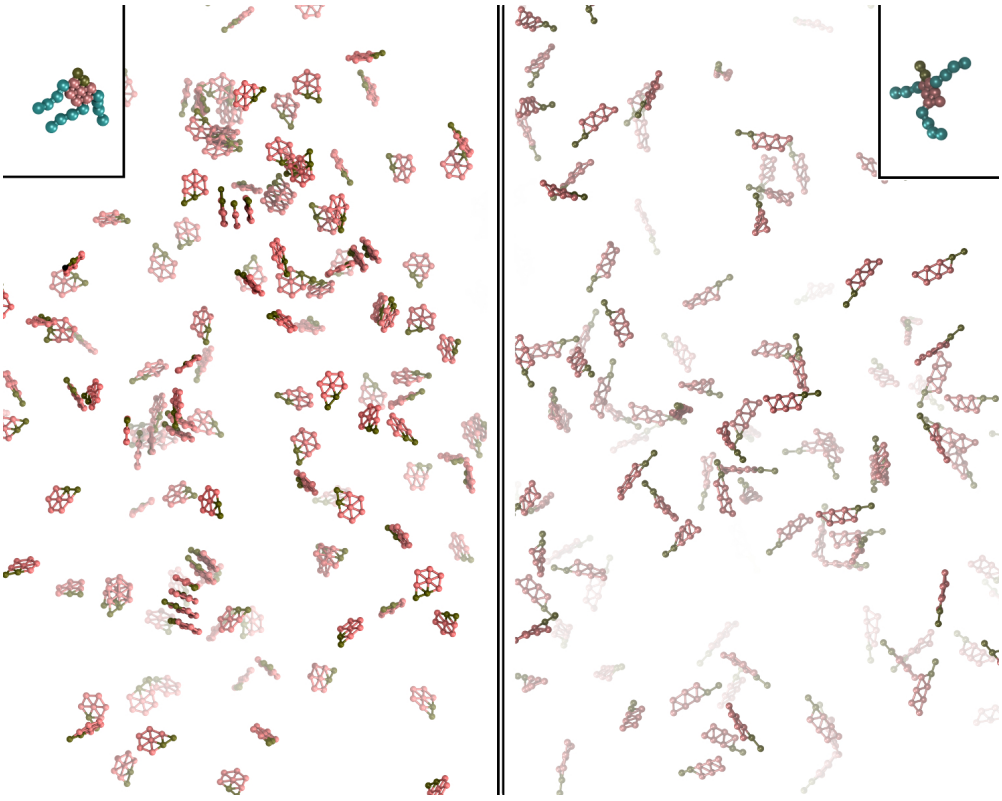

Figure 14: Comparison of the model asphaltenes in heptane. Left: APCE with a circular core. Right: APCL with an elongated core. In both cases, the inset shows the usual coarse grained beads for the entire molecule, while the main figures shows only the aromatic beads and their bonds, with the diameter set to $0.5\sigma$ to make the visualisation clearer.

range to choose from, e.g. benzene, pyridine, toluene etc., and again we limit ourselves to just toluene. This combination, heptol, has been widely used in experimental studies as a model system in which asphaltenes can be dissolved (e.g. refs. [132, 133, 134, 135, 136, 137, 138]). Heptol is the simplest solvent for asphaltenes where the aromatic to aliphatic ratio of the solvent can still be varied.

Given heptol as a base, the mixture ratio can be varied, and asphaltenes can be added to the system in varying concentration. Previous work [132] has indicated that a heptol ratio around 70/30 gives the most stabilising (and thus most interesting) interfacial properties, so the 70/30 heptol mixture is used as a base fluid here. The temperature and pressure are set to 20°C and 1 bar, respectively. The asphaltene concentration is varied, to study the effect this has on the system.

It is notable that in all the simulations reported here, the systems are started from random initial conditions. In particular, the asphaltenes are not placed at the oil/water interface, but they are themselves interfacially active. The tuning of cross-interactions is as reported in Section 4.2 for the heptane-water and the toluene-water cross interactions. For the asphaltenes, the alkane tail-water cross interactions use the same $k_{ij}$ as for heptane-water, otherwise the cross-interactions have not been adjusted.

These studies using the various model asphaltenes were performed at different concentrations from 240 to 960 asphaltene molecules in 40 000 molecules of solvent (70/30 heptol), together with 160 000 molecules of water. These systems were simulated in the $NpT$ ensemble using an elongated simulation box with a 3:1:1 side ratio, and the desired state (20°C, 1 bar, oil/water phase-separated) was obtained. Subsequently, the system was evolved in the $NVT$ ensemble in order to let it equilibrate.

At this point, some remarks are in order with regards to the relaxation times in these systems, as compared to experiments. Looking at the time it takes to reach equilibrium for the interfacial tension in asphaltene-heptol-water systems in experiments (e.g. [136, 139]) the timescales are of the order of hours,

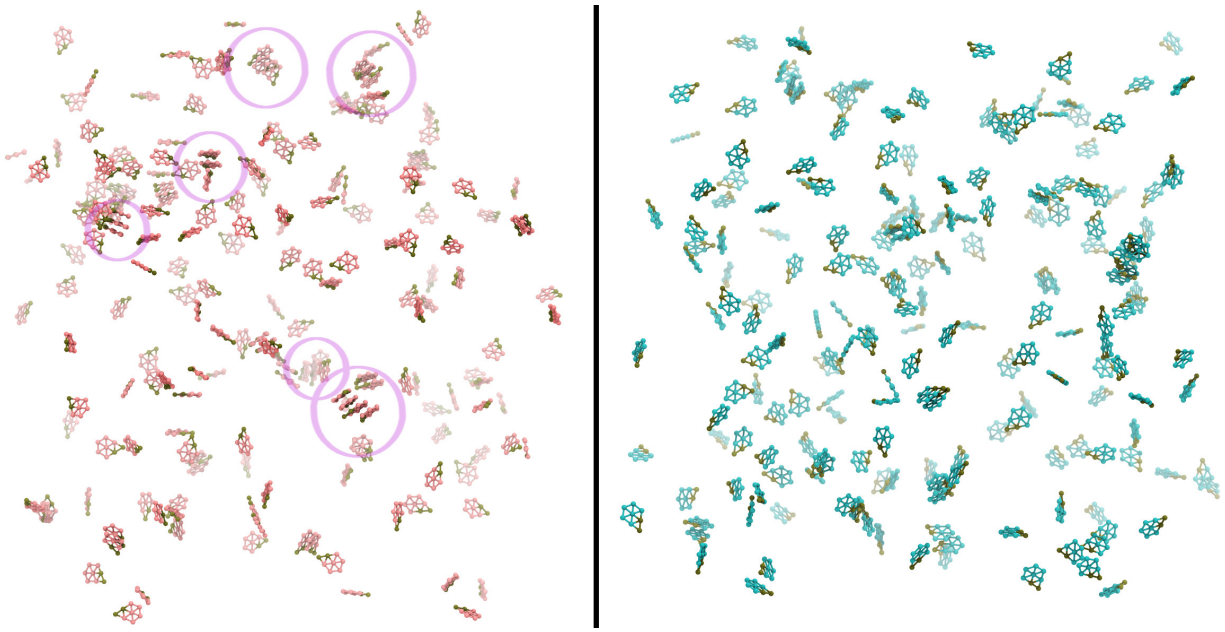

Figure 15: Comparison of the APCE model asphaltenes in heptane (left, red) and in toluene (blue, right). As in the previous figure, only the aromatic cores are shown. Purple circles highlight clusters with three or more molecules (there are none on the right-hand side). It is evident that the molecule is poorly soluble in heptane, where two-, three- and four-molecule clusters can be seen. In toluene, there is no clustering apart from the occasional contact between two asphaltene cores.

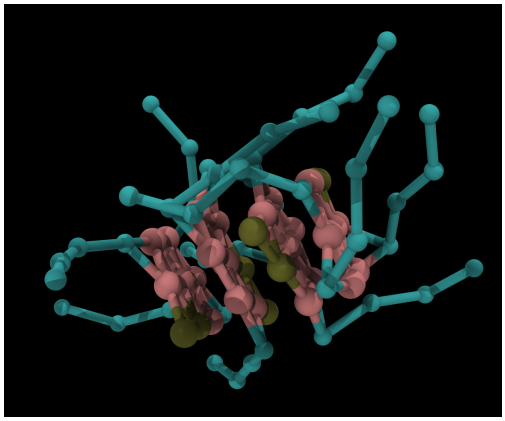

Figure 16: A closeup of a four-asphaltene APCE cluster in heptane. The beads are also here shown at reduced size for clarity; aromatic beads with diameter set to $0.5\sigma$ and alkane beads with diameter set to $0.25\sigma$. The colours indicate aromatic beads (red), pyridine beads (gold) and aliphatic beads (blue)

which is completely out of reach for molecular simulation. However, these long timescales are caused by the slow diffusion of asphaltene molecules from the far-away regions of the bulk to the asphaltene-depleted oil layer close to the interface. Moreover, these timescales are not representative of the situation when water drops travel through oil in a pipeline or a separator, where the ratio of the diffusion boundary layer width to the viscous boundary layer width, i.e. the Schmidt number, can be of the order of $10^6$, meaning that the speed of diffusion is increased by this order of magnitude for a falling drop as compared to a drop at rest in a tensiometer. Comparing this to the situation in simulations, it is clear that the diffusion cannot happen over a longer scale than the simulation box size, which is of the order of 10 nanometres. Experimental measurements indicate the diffusion coefficient of asphaltenes in solvents like heptol is of the order of $10^{-10}$ $\mathrm{m}^2/\mathrm{s}$ [140].

This means the characteristic time for an asphaltene to diffuse across the simulation box is of the order of $10^{-6}$ seconds.

There are two other relaxation time scales of importance, in addition to the time scale for diffusion. The second is the time scale for the adsorption of an asphaltene at the interface. With a coarse-grained description such as here, this time scale is very short, of the order of 1 nanosecond. The third is the time scale for reorientation of the asphaltenes at the interface, i.e. that those molecules already adsorbed find a tighter packing, which allows further molecules to adsorb at the interface. This time scale depends on how the asphaltenes associate at the interface, and is thus difficult to estimate *a priori*.

*5.1.1. Studies using the APCH model asphaltene*

The APCH model asphaltene was used in the first studies of asphaltene-heptol-water systems. Two concentrations were considered, namely 240 and 720 asphaltene molecules in 40 000 molecules of 70/30 heptol. The former corresponds to an asphaltene concentration of about 5%. Note that in these simulations, a simpler two-bead model for the toluene molecule [45] was used.

Snapshots of the oil-water interface from simulations at this lower concentration are shown in Figure 17. This figure shows the interface from the water side after 35 ns (left) and 350 ns (right). The water beads are not shown, and the solvent beads are shown only as grey outlines. It is seen from this figure that the interfacial configuration of asphaltenes changes during this time, with clusters forming at the interface. The number of asphaltenes at the interface increases by about 30% from 35 to 350 ns, and at 350 ns there are 0.25 molecules per square nanometre. Inspection of this system revealed that the interfacial adsorption left the bulk oil almost depleted of asphaltenes. Thus this situation with a lower concentration of asphaltenes is representative of a freshly-formed interface where diffusion has not yet had time to bring in more asphaltenes from the bulk.

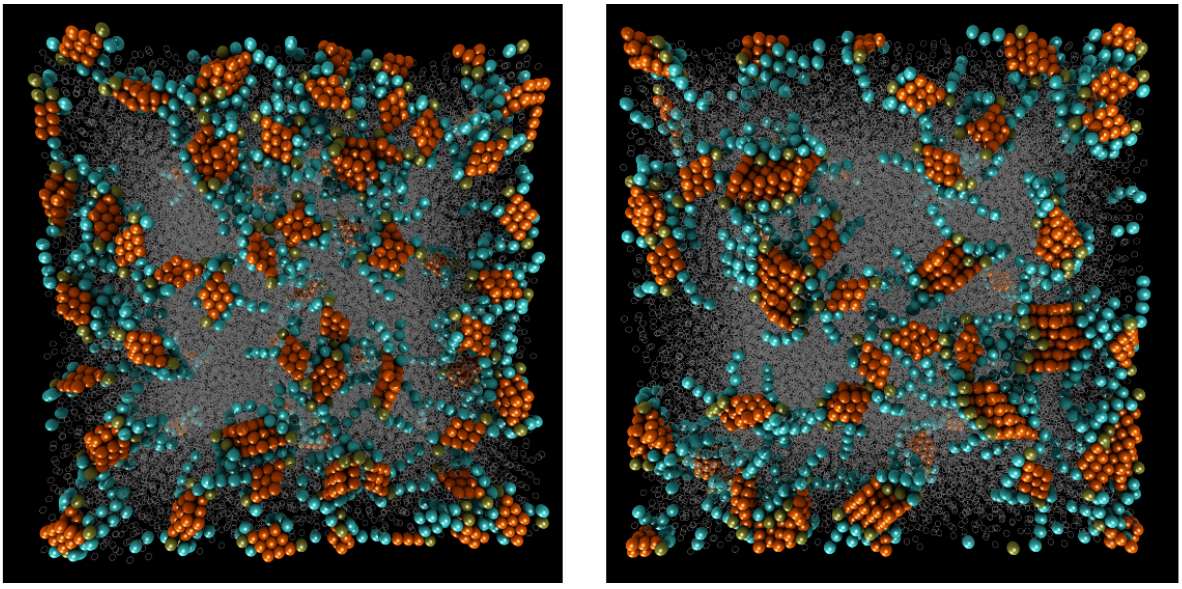

Figure 17: Snapshot of the interface seen from the water side, for the system with 240 APCH model asphaltenes after 35 ns (left) and 350 ns (right). Colours as in previous figures. Water molecules are omitted for clarity, and the heptane and toluene beads are shown in gray.

As previously mentioned, the time scales for diffusion can be of the order of minutes and hours, which is not tractable in these simulations. However, the effect of diffusion may be taken into account by starting the simulation with an initially higher asphaltene concentration. The higher concentration case, using 720 asphaltene molecules, gave about 5% asphaltenes remaining in the bulk after 350 ns, and is thus representative of the same system having reached equilibrium after diffusion from the bulk. Snapshots of this system are

shown in Figure 18, again with 35 ns at the left and 350 ns at the right. Again, there is an increase of about 30% in the number of adsorbed asphaltenes from 35 to 350 ns, and at 350 ns there are 0.5 molecules per square nanometre. It is evident from the snapshot that these asphaltene molecules are highly self-associative at the interface, i.e. that they cluster together. It is likely that this behaviour is not representative of real asphaltenes, which are believed to adsorb with the aromatic core towards the water [141].

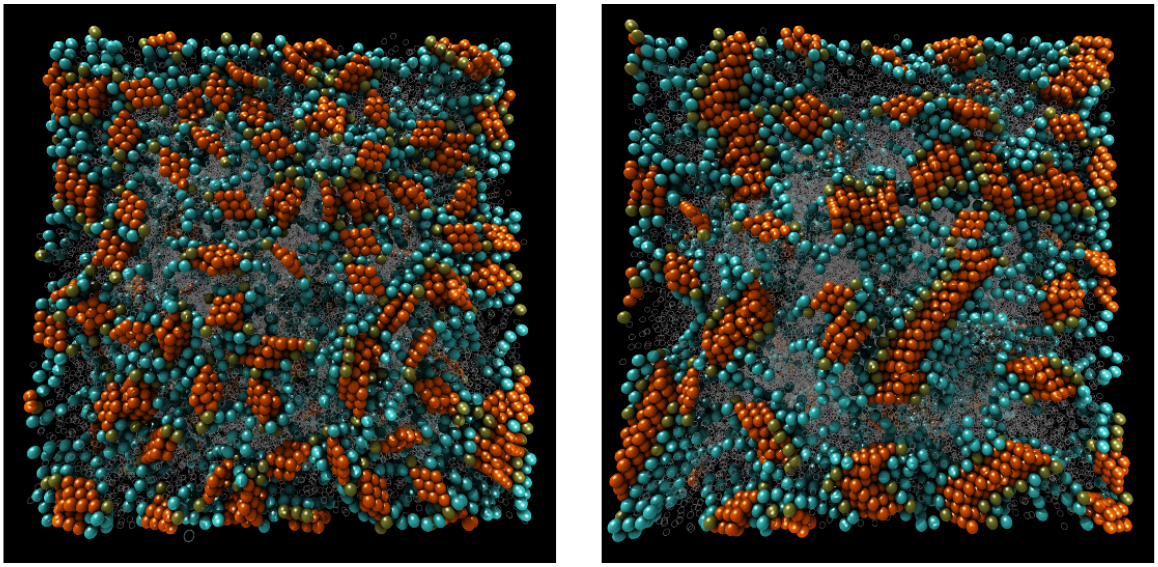

Figure 18: Same as the previous figure, for the system with 720 APCH asphaltene molecules. At this higher concentration, the tendency for the asphaltenes to cluster together at the interface is even more pronounced.

For the system with 720 asphaltene molecules at 350 ns, the interfacial tension and elasticity was calculated using the previously described methods. The interfacial tension was found to be 39.5 $\pm$ 1 mN/m. The elasticity was estimated to be 15 $\pm$ 10 mN/m; in Figure 19 the change in tension versus the change in interfacial area is shown together with a line showing the 15 mN/m slope.

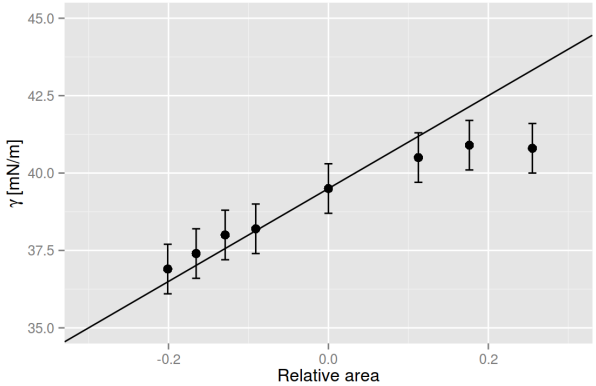


Figure 19: The change in interfacial tension versus the relative area $A/A_0 - 1$ for compressions (negative relative area) and expansions of the interface. It is seen that compressions give a reasonable elastic behaviour, but under expansion the change in tension levels off. The line corresponds to $K_a = 15$ mN/m.

*5.1.2. Studies using the APCE model asphaltene*

As previously mentioned, the new model asphaltenes were developed partly in response to the APCH model asphaltenes being more self-associative than what is expected based on experimental evidence. The APCE asphaltenes adopt a very different configuration at the interface, namely with the polycyclic aromatic core aligned with the water interface, and the aliphatic tails stretched back towards the oil phase. This is shown in Figure 20. In this figure, the interface is seen from the water side, in the system with 240 model asphaltenes after 50 ns of equilibration. In the centre, highlighted by green planes above and below, the interface is shown with the asphaltene molecules as in the previous figures. On the left side, a periodic image is shown with only the aromatic cores. On the right side, a periodic image is shown with only the aliphatic tails. In all three images, grey beads indicate heptane and toluene. It is seen that the aliphatic tails are protruding into the grey oil phase, indicated by the shadows these beads are casting on each other. In Figure 21, the same illustration is shown for the system with 720 asphaltene molecules.

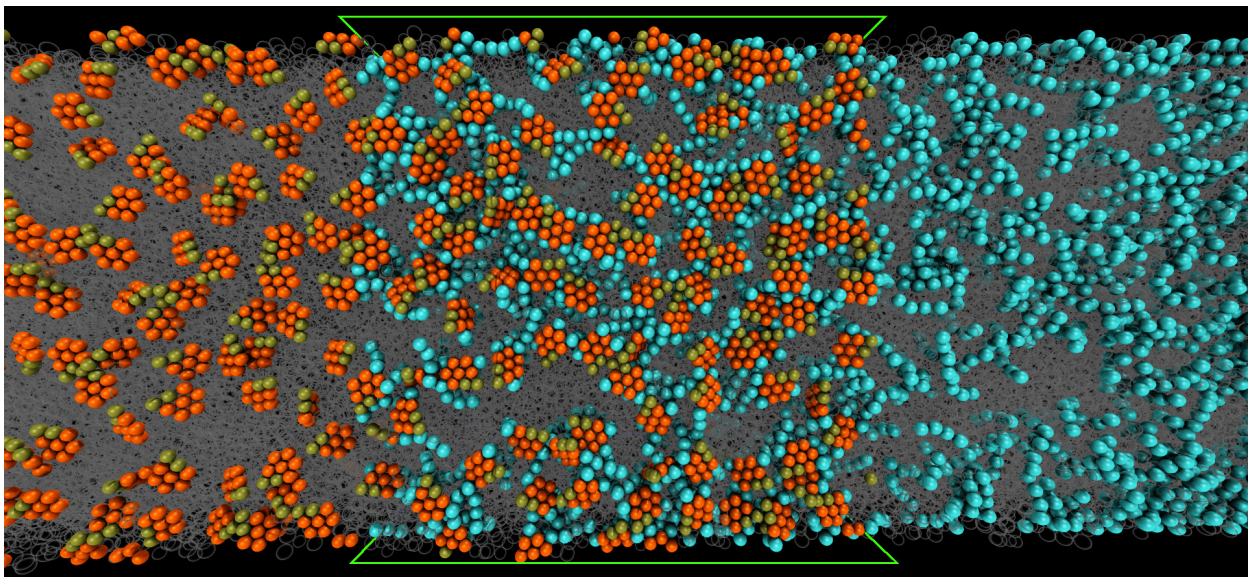

Figure 20: Snapshot of the APCE model asphaltene at the interface seen from the water side, for the system with 240 asphaltenes, after 50 ns of equilibration. Colors as in previous figures. On the right and left sides, periodic images of the interface are shown, where the aromatic cores and the aliphatic tails are omitted, respectively. It is seen that the aromatic cores are predominantly oriented in parallel with the interface, while the aliphatic tails are pointing away into the oil phase.

These results are in very good agreement with experiments performed by Andrews et al. [141] using sum frequency generation (SFG) spectroscopy to study the orientation of real asphaltenes at interfaces. They find that "SFG clearly indicates that asphaltene polycyclic aromatic hydrocarbons are highly oriented in the plane of the interface and that the peripheral alkanes are transverse to the interface." When comparing Figure 17 to Figure 20, it is clear that the APCE model asphaltene has an interfacial behavior closer to that observed in experiments, while results with the APCH model asphaltene show a qualitatively different interfacial orientation. It is noteworthy that previous atomistically detailed molecular simulations [124, 125, 126] have shown similar interfacial behaviour to the APCH model, i.e. have found the asphaltenes to be highly associative at the interface and stacking with cores orthogonal to the interface, in contrast with the experimental findings using real asphaltenes. Thus the results presented here with the APCE model asphaltene are the first simulations to be consistent with the experimental results from SFG spectroscopy [141].

This absence of clustering at the interface means that there is no long time scale for reorientation at the interface, unlike with the APCH asphaltenes. This means that extending simulation runtimes to 350 nanoseconds, as for the APCH asphaltenes, is not necessary. To confirm this, a simulation with the highest number of asphaltene molecules considered here was run until 150 ns, and no change in configuration was

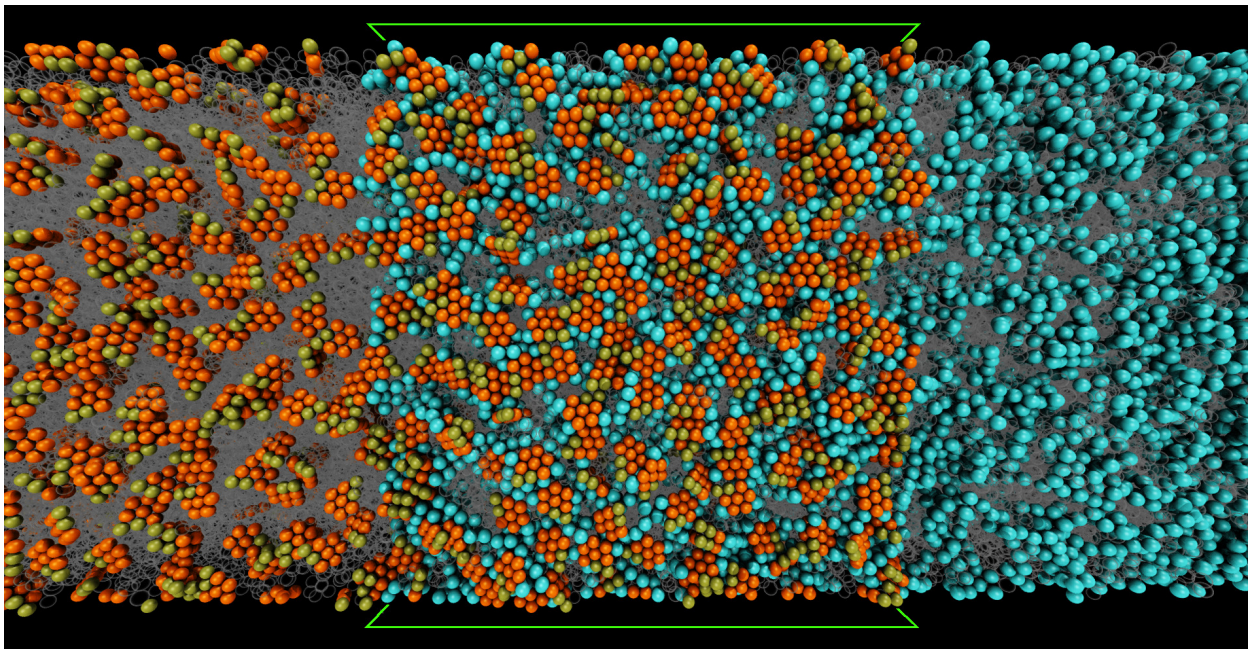

Figure 21: Same figure as Figure 20 for the system with 720 asphaltene molecules. It is seen that even at this high concentration, the asphaltenes show essentially no clustering at the interface. Some asphaltenes here have their cores oriented perpendicularly to the interface, but the great majority still have cores parallel to the interface.

observed between 50 and 150 ns.

With this model giving the interfacial behaviour as expected from experiments, it is interesting to see how the interfacial tension varies with the asphaltene concentration. This is plotted in Figure 22. It is seen that adding asphaltenes to the system decreases the interfacial tension, with what appears to be an exponentially decaying trend. Note that the concentration in this figure is given as the number of molecules, since interpretation of this number into bulk concentration is not immediately obvious. The variation in the number of molecules in the simulation can be interpreted either as snapshots in time during the diffusion process for one bulk concentration, or as the equilibrium interfacial tension for varying concentration of asphaltenes. In general, these values and variation in interfacial tension corresponds well with experimental observations, e.g. in [142].

The interfacial elasticity was also estimated with this model, using the system with 720 molecules after 50 ns, and found to be $55 \pm 20$ mN/m. The variation in tension with the interfacial area is shown in Figure 23, together with a line having a slope of 55 mN/m.

### *5.2. Macroscopic simulations of the draining of water drops in oil*

Given the immense potential for variations in even model crude oil/water systems, and the uncertainties still surrounding the asphaltenes despite the use of state-of-the-art analytic chemistry techniques, it is not possible in the experimental literature to provide enough detail for an exact comparison to be made here between simulations and experiments. It is also noteworthy that the elasticity as defined here has not been given consideration in the experimental literature. There, studies of interfacial properties in crude oil/water systems have either focused on the shear rheology (e.g. [143, 144]), or in the cases where dilatational elasticity has been considered (e.g. [145, 146, 147]), the authors have presupposed this elasticity to be of the type considered by Gibbs in his seminal work [3]. As we will demonstrate in the following, a Gibbs-type elasticity cannot cause the phenomena observed in experiments, for several reasons: Gibbs elasticity is given as the change in interfacial tension when a change in area causes a change in the concentration of a surface-active material. It follows that this elasticity is isotropic by definition, and furthermore that it cannot reduce the

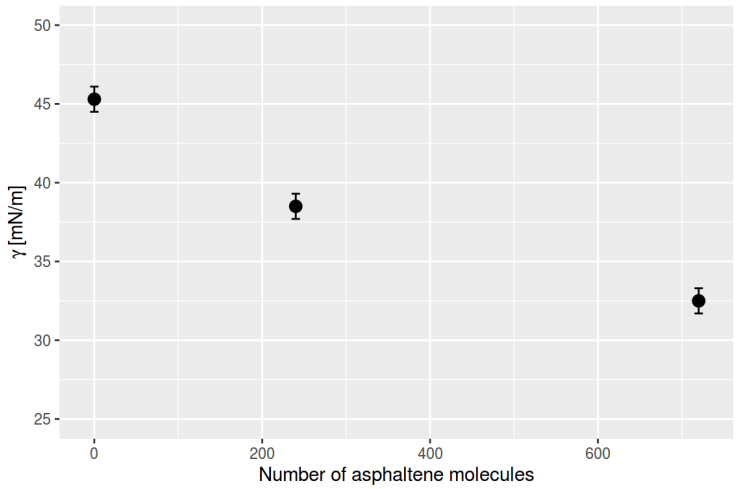


Figure 22: The interfacial tension $\gamma$ computed from molecular simulations, for varying concentration of asphaltenes. The decrease in $\gamma$ with increasing asphaltene concentration corresponds well with experimental measurements.

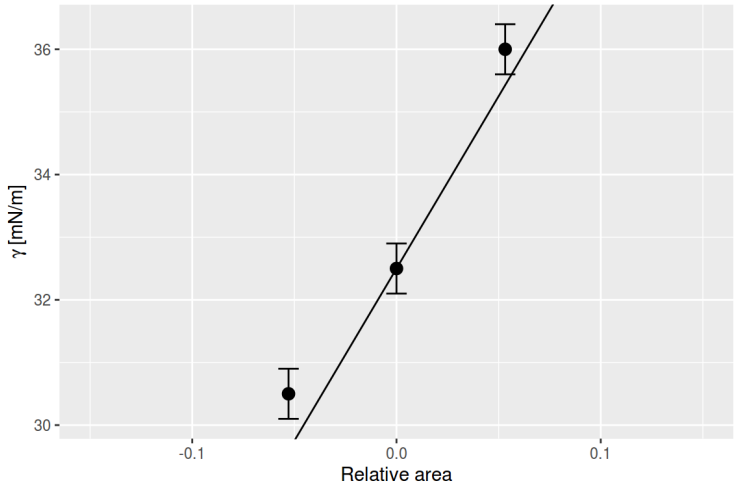


Figure 23: The change in interfacial tension versus the relative area $A/A_0 - 1$ for compression (negative relative area) and expansion of the interface, with the 720 asphaltene molecule system. It is seen that the behaviour is linear, i.e. elastic. The line corresponds to $K_a = 55$ mN/m.

tension to zero. The reader is referred to pp. 467–482 of the very readable paper by Gibbs [3] for further details.

All in all, these facts imply that our comparisons with experiments must be of the qualitative kind. A very interesting case for qualitative comparisons is the crumpled drop phenomenon, which occurs when a water drop in crude oil is drained by use of a needle. The appearance of wrinkles or crumples in the drop interface upon contraction is clearly evident in photographs and is thus not subject to interpretation, and it is a phenomenon fundamentally different from those observed in water/oil/surfactant systems.

In the experimental literature there are two different categories of experiments with draining water drops in crude-oil (or model systems). The first category concerns the micropipette experiments as reported e.g. by [13]. In this case, the drop size is representative of drops found in a real water/crude-oil emulsion, with a drop diameter of 50 $\mu$m. For these drops, buoyancy effects are small when compared to tension effects. In the second category of experiments the pendant drop tensiometer is employed, with much larger drops of

diameter around 5 mm, e.g. as reported by Pauchard et al. [14][3]. In this case, buoyancy effects are larger and tension effects smaller than in the micropipette case.

To get a quantitative measure of this difference, we may consider the Eötvös number, using the inverse drop curvature $1/\kappa$ as the length scale, i.e.

$$Eo = \frac{\Delta\rho g}{T\kappa^2} \tag{44}$$

where $\Delta\rho$ is the water-oil density difference in kg/m$^2$, $g = 9.81$ m/s$^2$ is the gravitational acceleration, and $T$ is the total tension, which is of the order of 0.01 N/m. This means the Eötvös number is $Eo \approx 5 \cdot 10^{-5}$ for the micropipette case, while it is $Eo \approx 0.5$ for the pendant drop case, meaning that in the former case buoyancy is completely negligible, while in the latter case buoyancy has an effect. This means that in the latter case, the interface is deformed both by the action of the tensiometer and by the effect of buoyancy.

*5.2.1. The pendant drop case*

With this in mind, we consider first the situation analogous to the pendant drop tensiometer, where drops are influenced both by buoyancy and by tension effects. In the experiments reported e.g. in [14], the drop remains axisymmetric up to the point of crumpling. It is seen that the crumpling only occurs in the azimuthal direction, thus the interface remains in tension in the meridional direction. This is due to the negative buoyancy of the water drop in oil. The situation can be compared to wrapping a handkerchief around an apple and lifting the corners of the handkerchief together: the cloth will wrinkle in the azimuthal direction, but there will obviously be tension in the meridional direction, since the cloth supports the weight of the apple.

After crumpling has occurred, as long as the crumple depth remains small compared to the drop radius, the axisymmetric simulation remains valid also in the crumpled region [71], where the interface then corresponds to an azimuthal mean interface. This is precisely because the azimuthal tension is zero in the crumpled region, and so this tension (including the effect of azimuthal curvature of the crumples) does not exert a force. Thus axisymmetric simulations can provide insight into this situation. Unfortunately, neither drop diameters prior to deflation, nor the composition (and thus density) of the oil phase, are given in [14]; moreover, the interfacial elasticity is not known, and thus an exact comparison to these experiments cannot be made.

The case considered is a drop of water with an initial diameter of 6.6 mm immersed in oil ($\rho_2 = 830$ kg/m$^3$) and attached to a needle which sucks the water out at a rate of 0.059 mL/s. The initial drop volume is 1.2 mL. The penalisation method is used to enforce no flow inside the needle walls, and a Pouseille flow inside the needle. There is no explicit handling of the drop/needle contact angle, but the interface inside the needle wall is forced to remain in its initial position by the penalisation. With this approach, the drop interface overlaps with the needle walls, as seen in the following Figures 24 and 26. Since the flow field is forced to be zero inside the walls, the interface points inside the walls (including at the needle wall boundary) will not move. This gives the effect of pinning the contact line location, but leaving the contact angle free to vary according to the drop interfacial dynamics.

The tension in this case is given by $\gamma = 30$ mN/m and $K_a = 50$ mN/m. These specific values are chosen based on the results from the molecular simulations, which have some uncertainty; further details are given in Table A.6. Thus the Eötvös number for the initial condition (where $T = \gamma$) is $Eo = 0.61$, and the simulation corresponds very well to the pendant drop regime.

As the simulation begins, the drop starts to fall, and a balance is quickly established between the drop tension and the drop negative buoyancy, forming a pendant drop. As the needle removes water from the drop, it shrinks, and eventually the "neck" of the drop has shrunk to the point that it becomes tensionless in the azimuthal direction, i.e. $T_\phi = 0$. This is shown in Figure 24.

In this plot, the axisymmetric drop profile is mirrored around the symmetry axis, and the tensions $T_s$ and $T_\phi$ are shown on the right- and left-hand sides, respectively, as colours on the interface. Inside and outside the drop, contours of the pressure field are shown. It is evident that even though $T_\phi$ is zero along a portion of the interface, there is still a pressure jump across the interface. It is also seen that the pressure difference

[3]The drop diameter is not given in this publication, but the tensiometer needle outer diameter is given as 1.65 mm.

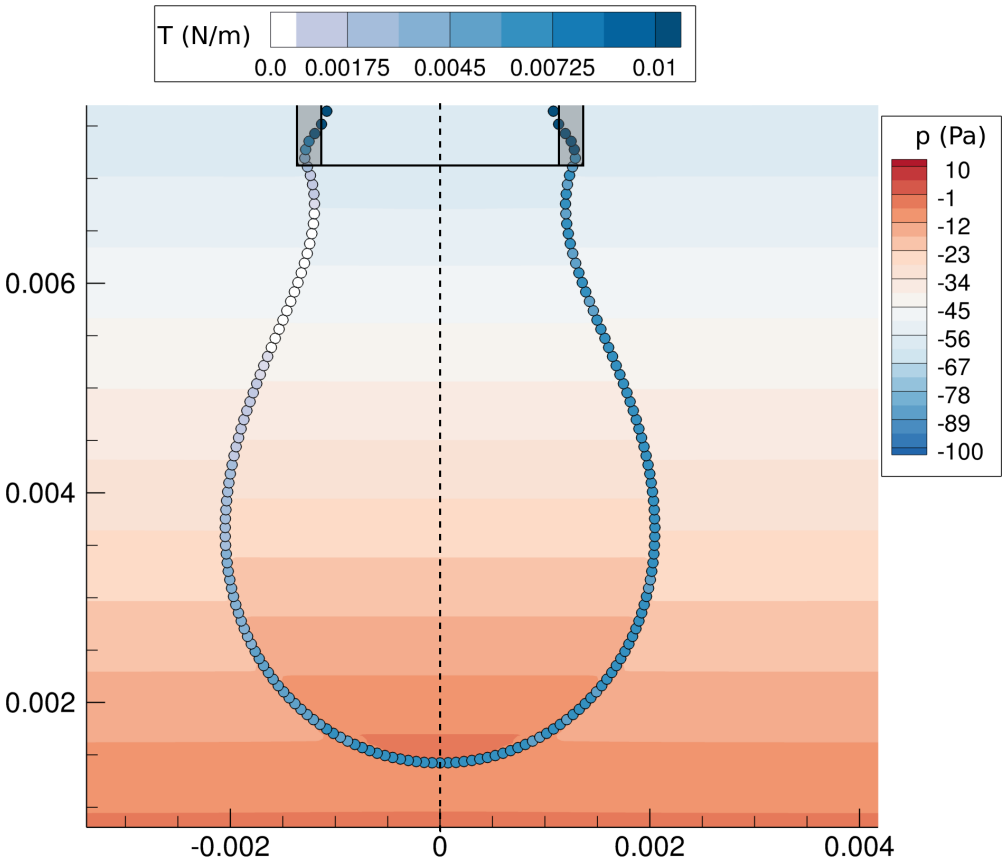


Figure 24: The axisymmetric drop profile (points) mirrored across the symmetry axis (dashed line). Only every 20th Lagrangian point is shown. The colour of the points corresponds to $T_s$ on the right-hand side and $T_\phi$ on the left-hand side of the plot. The pressure is as coloured contours inside and outside the drop, showing the varying pressure jump across the interface.

varies along the interface, since $T_\phi$ varies in the meridional direction; and as previously pointed out, there *cannot be* a force which cancels out this variation. This is true even in the static situation.

To compare the simulation result to images from experiments e.g. in [14], it is illustrative to construct a three-dimensional representation from the axisymmetric interfacial profile. To this end, the axisymmetric profile was imported into the Blender 3D graphics software and revolved around the symmetry axis to create a whole drop. Crumples were then inserted manually in the region where $T_\phi = 0$. Raytracing was used to create a realistic rendering of the drop and the needle to which it is attached. The result is shown in Figure 25 next to the experimental result from [14]. The similarity is striking, indicating that elasticity in the interface is a very likely explanation of the crumpled drop phenomenon seen in experiments.

*5.2.2. The micropipette case*

Considering the small Eötvös number regime, analogous to the micropipette drops, the situation after crumpling occurs is clearly not axisymmetric, and thus full three-dimensional simulations are required for quantitative studies of this. While the hybrid method discussed in this paper is readily extendable to three dimensions, this has not been done here due to time constraints, but may be considered in future work. One can, however, study this case from the qualitative perspective by considering a purely two-dimensional simulation, corresponding to a drop and pipette which are significantly elongated in one direction (perpendicular to the simulation domain).

The case considered for this case was with an initial diameter of 2 mm, corresponding to $Eo = 0.06$. While this drop (and $Eo$) is substantially larger than in the experiments, it is small enough that gravity

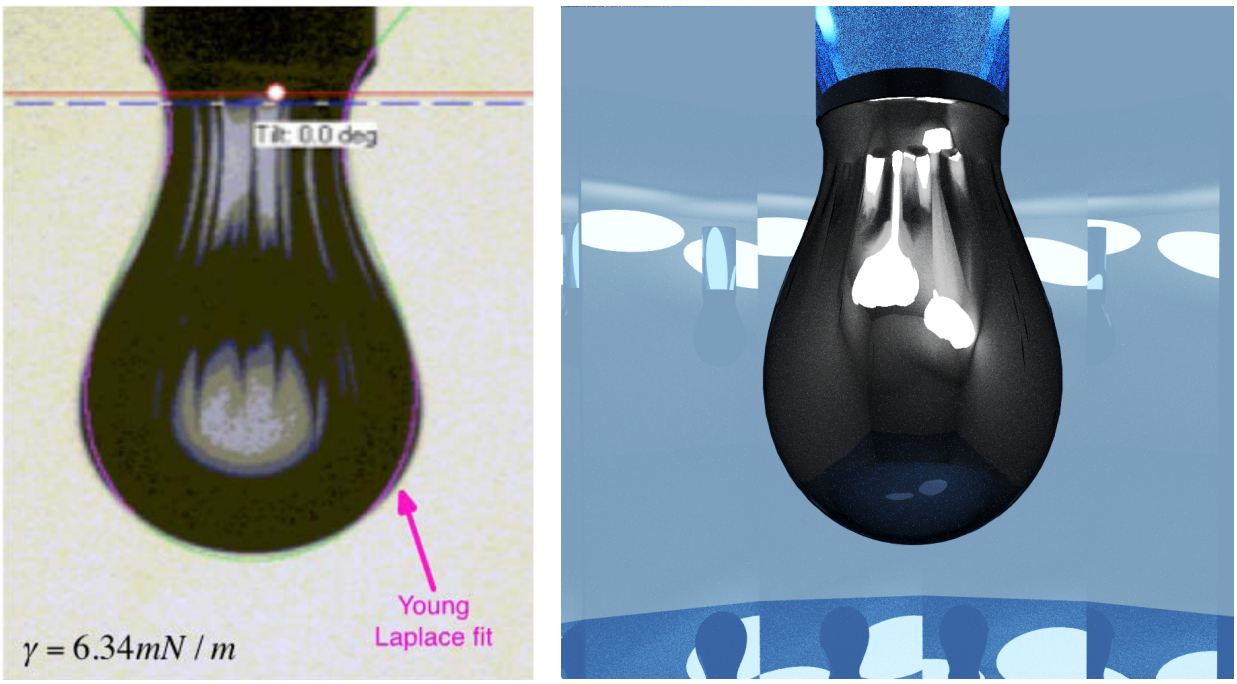


Figure 25: Right: raytrace of the drop profile from simulations, revolved around the symmetry axis and with crumples inserted into the region where $T_\phi = 0$. Left: experimental result showing a deflated asphaltene-stabilised water drop in oil. (Left figure reprinted with permission from: V. Pauchard, J. P. Rane, S. Banerjee, Asphaltene-laden interfaces form soft glassy layers in contraction experiments: A mechanism for coalescence blocking, Langmuir 30 (2014) 12795–12803. Copyright (2014) American Chemical Society.)

becomes unimportant. Accordingly, the simulation is with zero gravity. Further details of the case are given in Table A.7; see also [90]. A comparison of the simulation result with the photograph from experiments by Yeung et al. [13], both from after crumpling has occurred, is shown in Figure 26. A good qualitative similarity between the two is seen.

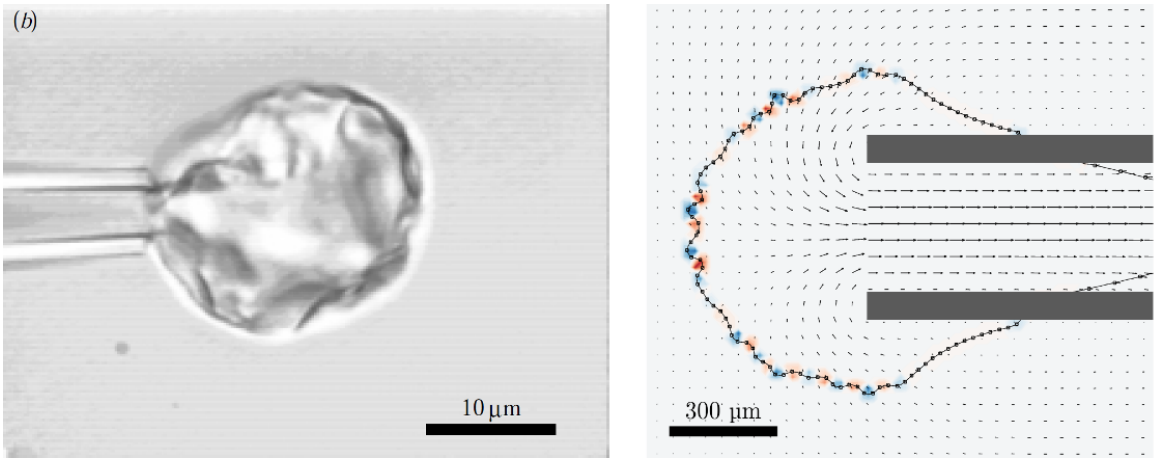


Figure 26: Right: two-dimensional simulation, with red and blue colours indicating interfacial curvature. Velocities are plotted for every 5th grid point and every 10th Lagrangian point is plotted. Left: experimental result showing the crumpled drop attached to a micropipette. (Left figure reprinted with permission from: A. Yeung, T. Dabros, J. Czarnecki, J. Masliyah, On the interfacial properties of micrometre–sized water droplets in crude oil, Proceedings of the Royal Society of London A (1999) 3709–3723.

## 6. Discussion

This paper presents a multiscale approach to simulations that shed light on the behaviour of asphaltene-covered water drops in crude oils. The simulation results at both the molecular and at the continuum scale showcase several interesting phenomena which appear in these systems. Ultimately, a better understanding of these phenomena will lead to a better understanding of crude oil/water emulsions, which are made up of trillions of tiny water drops, each covered with asphaltene molecules. This improved understanding can be utilised to reduce the cost and footprint of oil-water separation equipment, as well as to reduce the use of chemicals and heat in these separators. This in turn leads to reductions in both capital and operational expenses, as well as reduced emissions from oil production.

In the molecular simulations it is found that coarse-grained model asphaltenes are highly sensitive to the molecular architecture, to the point that molecules which are isomers both on the atomistic and on the coarse-grained scales have very different solubilities in the solvents in question (heptane and toluene). This is consistent with e.g. the findings by Sedghi et al. [122] who found in their atomistic simulations that small variations in the side groups of model asphaltenes caused large differences in solubility.

It is notable that the two solvents in question, heptane and toluene, are not very different in the first place: they are miscible, have the same number of carbon atoms, and have similar Hildebrand solubility parameters[4], 15.3 and 18.3 respectively, compared to e.g. 26.2 for ethanol and 48.0 for water, all these from [148] given in $\mathrm{MPa}^{1/2}$. The most obvious difference between heptane and toluene is the different molecular architecture of the two (ring-shaped and linear), which in turn enables toluene to have $\pi$-orbital interactions with other aromatic molecules. With the similarity in mind, an interesting question arises: Asphaltenes are known to be a highly complex mixture of different molecules, which originate as part of the well-stream from crude oil reservoirs deep underground. Unlike the carefully synthesised molecules used in man-made chemical processes, asphaltenes are created in an essentially random fashion. How, then, do they achieve such a detailed solubility balance?

It is likely that the explanation lies in a two-fold application of an argument analogous to the "anthropic principle": the fact that asphaltenes are insoluble in heptane comes from their penchant for $\pi$-$\pi$ ring interactions, which cause them to cluster and subsequently fall out of solution. If the molecules had smaller aromatic cores, they would not show this behaviour, but then they would also not be asphaltenes in the first place, rather they would be resins. The solubility in toluene can be understood from a similar point of view: were the asphaltenes not soluble in toluene (or aromatic solvents in general), they would not be soluble in crude oil at all, so they would never be found in the flow coming up from the reservoir.

An interesting possible topic for investigation in future studies is the effect of asphaltene polydispersity, which is an obvious next step on the path towards better models for molecular simulations involving asphaltenes. A very appealing idea is the construction of a coarse-grained QMR method, which would in principle enable the construction of an arbitrary number of different coarse-grained model asphaltene molecules.

When the model asphaltenes are introduced into the heptol-water system, they are found to intrinsically be interfacially active. No tuning has been done of the cross-interactions between the aromatic cores and water, due to the lack of experimental properties to tune this interaction to. With this in mind, it is remarkable how well the interfacial behaviour of particularly the APCE model asphaltenes matches what one expects based on our understanding of the $\pi$-interactions between aromatic rings and water [149].

The molecular simulations presented here using the APCE model asphaltenes are the first reported simulations of asphaltenes in oil-water systems which obtain the correct interfacial behaviour, as compared to experimental results using sum frequency generation spectroscopy [141]. This leads one to speculate that perhaps a coarse-grained model asphaltene which has the correct solubility behaviour in heptane and in toluene, such as the APCE model, somehow begins to take the asphaltene polydispersity into account through the coarse-grained nature.

When it comes to the pendant drop case, simulations highlight that the tension is highly anisotropic, and that the azimuthal tension varies significantly along the drop profile, being zero around the neck of the

[4]The Hildebrand solubility parameter is a quantity most useful for comparing solvents, and is given by the square root of the cohesive energy density.

drop when volume has been removed with the needle. This is caused by the Eötvös number being close to one, such that both gravity and the needle suction are responsible for deforming the drop. The resulting variations in the tensions explain the axisymmetric crumpling observed in experiments.

An important implication of the anisotropy in the tension is that when using the pendant drop tensiometer to study asphaltene covered drops, it makes little sense to speak of a "surface pressure" as a scalar number indicative of the total tension in the interface. This is in contrast to the situation with a flat interface, as in a classical Langmuir-Blodgett trough apparatus, where the surface pressure would remain well-defined. This questions the findings in previous studies where conclusions are drawn on the basis of variations in the "surface pressure" of asphaltene-covered drops measured using the pendant drop tensiometer to deform drops. It is also important to note that the elasticity considered in these simulations is fundamentally different from the Gibbs elasticity of surfactants.

When studying ordinary surfactants, the Marangoni effect ensures that (at equilibrium) the distribution of surfactants on the drop interface is uniform, and it thus makes sense to speak of a surface pressure in this case. For the anisotropic tensions studied here, the analogue of the Marangoni effect serves only to remove variation of $T_s$ in the meridional direction etc. But as discussed previously, it is not possible to have forces acting to cancel the variation in $T_\phi$ along the meridional direction, since these forces would be in the direction binormal to the axis of strain.

When it comes to the micropipette drop case, the Eötvös number is $Eo \ll 1$, and thus gravity is unimportant. This means that the tension forces dominate, and that drop deformations are entirely controlled by the needle suction. This causes the drop to remain spherical up to the point of crumpling, such that the crumples appear simultaneously across the drop interface. The two-dimensional simulation at low Eötvös number demonstrates a qualitative similarity to this, in that crumpling appears on all of the interface.

How these macroscopic phenomena relate to emulsion stability remains a topic for future investigations. An important question which should be investigated is the deformation of emulsion drops as they travel from the point of emulsion formation, through the varying turbulence levels in the flow which transports them through the pipeline, and finally when they end up in the oil-water separator, where the flow is less turbulent and the drop shapes will be spherical. Taking this into account, together with the adsorption time scales for asphaltenes in a highly sheared flow, would provide important insight into the situation for real emulsion drops. The multiscale method employed here, with future extensions e.g. to fully three-dimensional flow, is uniquely poised to help answer these and other important questions.

## 7. Concluding remarks

To summarise, the current paper presents a multiscale approach to the simulation of drops with complex interfaces, such as water drops in crude oil which are covered with asphaltene molecules. The approach combines coarse-grained molecular dynamics simulations using the SAFT-$\gamma$ Mie force field, with detailed two-phase flow simulations using a hybrid level-set/ghost-fluid/immersed-boundary method developed as part of this work. At the molecular scale, the coarse-grained approach enables simulations at unprecedented time- and length-scales, using accurate models for both the simple fluids and the complex asphaltene molecules. The interfacial tension $\gamma$ and elasticity $K_a$ are estimated, for use in the macroscopic simulations.

At the macroscopic scale, detailed simulations of oil-water interfaces with both interfacial tension and elastic properties shed new light on experimental results that showcase one of the peculiarities of complex fluid-fluid interfaces, namely crumpling drops. Two categories of experimental results exist in the literature, with different classes of crumpling behaviour. The results presented here demonstrate that this difference is caused by the large difference in Eötvös number between the two categories. In the pendant drop case, with an Eötvös number around one, both gravity and the experimental setup are responsible for deforming the drop, and this combination leads to an axisymmetric crumpling regime. In the micropipette case, with an Eötvös number much smaller than one, the drop remains spherical up to the point of crumpling, leading to a fully three-dimensional behaviour.

These results present a novel hypothesis, namely anisotropic tensions in the interface, as an explanation of the crumpling phenomenon. This hypothesis is different from previously suggested explanations, e.g. that

based on glass transitions in [14]. The hypothesis put forward in this work makes fewer assumptions and has greater predictive power than those presented in previous works.

Building on this work, there are numerous avenues open for future investigations. The effect on interfacial properties of crude oil composition, asphaltene polydispersity, asphaltene architecture, other crude components such as resins, etc., should all be considered. Extending the hybrid simulation method to three dimensions would enable not just simulations of e.g. the micropipette drops, but also of drops in more complicated (even turbulent) flows. Furthermore, the extension to drop coalescence is a very interesting topic. Also, this study assumes that the interfacial elasticity is of the Hookean type. While this is the simplest form of elasticity, it could well be that asphaltene-covered interfaces can be more accurately modelled using e.g. a neo-Hookean elasticity.

All in all, the methods presented here are well suited for increasing our understanding of dispersed two-phase flows with complex interfaces. This is important not just for the application in focus here, crude oil/water systems, but also for biological systems such as the flow of blood or the transport of proteins, and for chemical processes involving multiphase flow and macromolecules.

## Acknowledgements

ÅE, STM and BM acknowledge the financial support from the project *Fundamental understanding of electrocoalescence in heavy crude oils* coordinated by SINTEF Energy Research and funded by the Petromaks programme of the Research Council of Norway (206976), Petrobras, Statoil and Wärtsilä Oil & Gas Systems.

EM acknowledges the financial support for the Molecular Systems Engineering group from the Engineering and Physical Sciences Research Council (grant numbers EP/E016340, EP/J014958, EP/L020564).

The authors would like to thank Prof. Edo Boek for fruitful discussions on these matters. The authors are also grateful for computational resources at the Imperial College High Performance Computing Service, and at the Abel cluster operated by the University of Oslo and the Norwegian metacenter for High Performance Computing (NOTUR), as well as assistance from the staff at both locations.

## References

[1] C. Marangoni, Sull'espansione Delle Gocce di un Liquido Gallegianti Sulla Superficie di Altro Liquido, Ph.D. thesis, University of Pavia, 1865.

[2] C. Marangoni, Über die Ausbreitung der Tropfen einer Flussigkeit auf der Oberfläche einer anderen, Annalen der Physik und Chemie 143 (1870) 337–354.

[3] J. W. Gibbs, On the equlibrium of heterogeneous substances, Transactions of the Connecticut Academy of Arts and Sciences 143 (1878) 337–354.

[4] Pliny, *Naturalis Historia*, Teubner, Leipzig, 1906. `http://penelope.uchicago.edu/Thayer/E/Roman/Texts/Pliny_the_Elder/home.html`.

[5] Pliny, Pliny's Natural History, Harvard University Press, Massachusetts, 1949. `http://www.masseiana.org/pliny.htm`.

[6] A. Pockels, Relations between the surface-tension and relative contamination of water surfaces, Nature 48 (1893) 152–154.

[7] B. Szyszkowski, Experimentelle Studien über kapillare Eigenschaften der wässerigen Lösungen von Fettsäuren, Zeitschrift für Physikalische Chemie 64 (1908) 385–414.

[8] I. Langmuir, The adsorption of gases on plane surfaces of glass, mica and platinum., Journal of the American Chemical Society 40 (1918) 1361–1403.

[9] A. Frumkin, On a simple method of testing the Gibbs concepts, Zeitschrift für Physikalische Chemie 116 (1925) 498.

[10] V. Levich, V. Krylov, Surface-tension-driven phenomena, Annual Review of Fluid Mechanics 1 (1969) 293–316.

[11] V. G. Levich, Physicochemical hydrodynamics, Prentice-Hall, 2nd edition, 1962.

[12] T. G. Fai, B. E. Griffith, Y. Mori, C. S. Peskin, Immersed boundary method for variable viscosity and variable density problems using fast constant-coefficient linear solvers i: Numerical method and results, SIAM Journal on Scientific Computing 35 (2013) B1132–B1161.

[13] A. Yeung, T. Dabros, J. Czarnecki, J. Masliyah, On the interfacial properties of micrometre–sized water droplets in crude oil, Proceedings of the Royal Society of London A: Mathematical, Physical and Engineering Sciences 455 (1999) 3709–3723.

[14] V. Pauchard, J. P. Rane, S. Banerjee, Asphaltene-laden interfaces form soft glassy layers in contraction experiments: A mechanism for coalescence blocking, Langmuir 30 (2014) 12795–12803.

[15] M. Boussingault, XCI. On the constitution of bitumens, Philosophical Magazine Series 3 9 (1836) 487–488.

[16] M. P. Hoepfner, Investigations into Asphaltene Deposition, Stability, and Structure, Ph.D. thesis, University of Michigan, 2013.
[17] A. A. Herod, K. D. Bartle, R. Kandiyoti, Comment on a paper by Mullins, Martinez-Haya, and Marshall "Contrasting perspective on asphaltene molecular weight. This comment vs the overview of A. A. Herod, K. D. Bartle, and R. Kandiyoti", Energy & Fuels 22 (2008) 4312–4317.
[18] G. C. Klein, S. Kim, R. P. Rodgers, A. G. Marshall, A. Yen, Mass spectral analysis of asphaltenes. II. Detailed compositional comparison of asphaltenes deposit to its crude oil counterpart for two geographically different crude oils by ESI FT-ICR MS, Energy & Fuels 20 (2006) 1973–1979.
[19] T. Jones, E. Neustadter, K. Whittingham, et al., Water-in-crude oil emulsion stability and emulsion destabilization by chemical demulsifiers, Journal of Canadian Petroleum Technology 17 (1978) –.
[20] O. V. Gafonova, H. W. Yarranton, The stabilization of water-in-hydrocarbon emulsions by asphaltenes and resins, Journal of Colloid and Interface Science 241 (2001) 469–478.
[21] J. Sjöblom (Ed.), Encyclopedic handbook of emulsion technology, CRC Press, 2001.
[22] S. L. Kokal, Crude oil emulsions: A state-of-the-art review., SPE Production & Facilities 20 (2005) 5–13.
[23] P. K. Kilpatrick, Water-in-crude oil emulsion stabilization: Review and unanswered questions, Energy & Fuels 26 (2012) 4017–4026.
[24] C. Dicharry, D. Arla, A. Sinquin, A. Graciaa, P. Bouriat, Stability of water/crude oil emulsions based on interfacial dilatational rheology, Journal of colloid and interface science 297 (2006) 785–791.
[25] J. Bi, F. Yang, D. Harbottle, E. Pensini, P. Tchoukov, S. Simon, J. Sjöblom, T. Dabros, J. Czarnecki, Q. Liu, Z. Xu, Interfacial layer properties of a polyaromatic compound and its role in stabilizing water-in-oil emulsions, Langmuir (2015). Article in Press.
[26] W. E, B. Engquist, Z. Huang, Heterogeneous multiscale method: A general methodology for multiscale modelling, Phys. Rev. B 67 (2003).
[27] A. Brandt, Multiscale and multiresolution methods: Theory and applications, Springer, Berlin, Heidelberg.
[28] S. Chapman, T. G. Cowling, C. Cercignani, The Mathematical Theory of Non-uniform Gases: An Account of the Kinetic Theory of Viscosity, Thermal Conduction and Diffusion in Gases, Cambridge Mathematical Library, 1991.
[29] E. A. Müller, K. E. Gubbins, Molecular-based equations of state for associating fluids: A review of SAFT and related approaches, Industrial & Engineering Chemistry Research 40 (2001) 2193–2211.
[30] I. G. Economou, Statistical associating fluid theory: A successful model for the calculation of thermodynamic and phase equilibrium properties of complex fluid mixtures, Industrial & Engineering Chemistry Research 41 (2002) 953–962.
[31] S. P. Tan, H. Adidharma, M. Radosz, Recent advances and applications of statistical associating fluid theory, Industrial & Engineering Chemistry Research 47 (2008) 8063–8082.
[32] C. McCabe, A. Galindo, SAFT associating fluids and fluid mixtures, Royal Society of Chemistry, London.
[33] T. Lafitte, C. Avendaño, V. Papaioannou, A. Galindo, C. S. Adjiman, G. Jackson, E. A. Müller, SAFT-$\gamma$ force field for the simulation of molecular fluids: 3. Coarse-grained models of benzene and hetero-group models of n-decylbenzene, Molecular Physics 110 (2012) 1189–1203.
[34] V. Papaioannou, T. Lafitte, C. Avendaño, C. S. Adjiman, G. Jackson, E. A. Müller, A. Galindo, Group contribution methodology based on the statistical associating fluid theory for heteronuclear molecules formed from Mie segments, The Journal of Chemical Physics 140 (2014) –.
[35] G. Mie, Zur kinetischen Theorie der einatomigen Körper, Annalen der Physik 316 (1903) 657–697.
[36] N. Ramrattan, C. Avendaño, E. Müller, A. Galindo, A corresponding-states framework for the description of the Mie family of intermolecular potentials, Molecular Physics (2015) 1–16.
[37] W. Noid, Perspective: Coarse-grained models for biomolecular systems, The Journal of chemical physics 139 (2013) 090901.
[38] E. Brini, E. A. Algaer, P. Ganguly, C. Li, F. Rodriguez-Ropero, N. F. A. van der Vegt, Systematic coarse-graining methods for soft matter simulations - a review, Soft Matter 9 (2013) 2108–2119.
[39] S. J. Marrink, H. J. Risselada, S. Yefimov, D. P. Tieleman, A. H. De Vries, The MARTINI force field: coarse grained model for biomolecular simulations, The Journal of Physical Chemistry B 111 (2007) 7812–7824.
[40] X. Periole, S.-J. Marrink, The martini coarse-grained force field, Biomolecular Simulations: Methods and Protocols (2013) 533–565.
[41] E. A. Müller, A. Mejía, Resolving discrepancies in the measurements of the interfacial tension for the CO2 + H2O mixture by computer simulation, The Journal of Physical Chemistry Letters 5 (2014) 1267–1271.
[42] C. Avendaño, T. Lafitte, A. Galindo, C. S. Adjiman, G. Jackson, E. A. Müller, SAFT-$\gamma$ force field for the simulation of molecular fluids. 1. A single-site coarse grained model of carbon dioxide, The Journal of Physical Chemistry B 115 (2011) 11154–11169.
[43] C. Avendaño, T. Lafitte, C. S. Adjiman, A. Galindo, E. A. Müller, G. Jackson, SAFT-$\gamma$ force field for the simulation of molecular fluids: 2. Coarse-grained models of greenhouse gases, refrigerants, and long alkanes, The Journal of Physical Chemistry B 117 (2013) 2717–2733.
[44] O. Lobanova, C. Avendaño, T. Lafitte, E. A. Müller, G. Jackson, SAFT-$\gamma$ force field for the simulation of molecular fluids: 4. A single-site coarse-grained model of water applicable over a wide temperature range, Molecular Physics 113 (2015) 1228–1249.
[45] A. Mejía, C. Herdes, E. A. Müller, Force fields for coarse-grained molecular simulations from a corresponding states correlation, Industrial & Engineering Chemistry Research 53 (2014) 4131–4141.
[46] C. Herdes, E. Forte, G. Jackson, E. Müller, Predicting the adsorption of n-perfluorohexane in BAM P109 standard activated carbon by molecular simulation using SAFT-$\gamma$ Mie coarse-grained force fields, Adsorption Science and Technology

33 (2015) –.
[47] C. Herdes, E. Santiso, C. James, J. Eastoe, E. Müller, Modelling the interfacial behaviour of dilute light-switching surfactant solutions, Journal of Colloid and Interface Science 445 (2015) 16–23.
[48] P. E. Theodorakis, E. A. Müller, R. V. Craster, O. K. Matar, Superspreading: Mechanisms and molecular design, Langmuir 31 (2015) 2304–2309.
[49] E. A. Müller, C. Herdes, T. S. Totton, Coarse-grained models for crude oils: A direct link between equations of state and molecular simulations, in: Offshore Technology Conference.
[50] M. P. Allen, D. J. Tildesley, Computer simulation of liquids, Oxford university press, 1989.
[51] D. Frenkel, B. Smit, Understanding molecular simulation: from algorithms to applications, volume 1, Academic press, 2001.
[52] B. J. Alder, T. E. Wainwright, Phase transition for a hard sphere system, The Journal of Chemical Physics 27 (1957) 1208–1209.
[53] B. J. Alder, T. E. Wainwright, Molecular motions, Scientific American 201 (1959) 113–126.
[54] K. Kadau, T. C. Germann, P. S. Lomdahl, Molecular dynamics comes of age: 320 billion atom simulation on BlueGene/L, International Journal of Modern Physics C 17 (2006) 1755–1761.
[55] G. Zhao, J. R. Perilla, E. L. Yufenyuy, X. Meng, B. Chen, J. Ning, J. Ahn, A. M. Gronenborn, K. Schulten, C. Aiken, et al., Mature HIV-1 capsid structure by cryo-electron microscopy and all-atom molecular dynamics, Nature 497 (2013) 643–646.
[56] Å. Ervik, G. J. Serratos, E. A. Müller, raaSAFT: a framework enabling coarse-grained molecular dynamics simulations based on the SAFT-$\gamma$ Mie force field, Submitted (2016).
[57] J. A. Anderson, C. D. Lorenz, A. Travesset, General purpose molecular dynamics simulations fully implemented on graphics processing units, Journal of Computational Physics 227 (2008) 5342 – 5359.
[58] J. Glaser, T. D. Nguyen, J. A. Anderson, P. Lui, F. Spiga, J. A. Millan, D. C. Morse, S. C. Glotzer, Strong scaling of general-purpose molecular dynamics simulations on GPUs, Computer Physics Communications 192 (2015) 97 – 107.
[59] G. J. Martyna, D. J. Tobias, M. L. Klein, Constant pressure molecular dynamics algorithms, The Journal of Chemical Physics 101 (1994) 4177–4189.
[60] W. G. Hoover, J. C. Sprott, P. K. Patra, Ergodic time-reversible chaos for Gibbs' canonical oscillator, Physics Letters A 379 (2015) 2935 – 2940.
[61] P. K. Patra, J. C. Sprott, W. G. Hoover, C. G. Hoover, Deterministic time-reversible thermostats: chaos, ergodicity, and the zeroth law of thermodynamics, Molecular Physics 113 (2015) 2863–2872.
[62] W. G. Hoover, An appreciation of Berni Julian Alder, arXiv preprint 1510.05897 (2015).
[63] J. G. Kirkwood, F. P. Buff, The statistical mechanical theory of surface tension, The Journal of Chemical Physics 17 (1949) 338–343.
[64] C. Vega, E. de Miguel, Surface tension of the most popular models of water by using the test-area simulation method, The Journal of Chemical Physics 126 (2007) –.
[65] W. K. den Otter, W. J. Briels, The bending rigidity of an amphiphilic bilayer from equilibrium and nonequilibrium molecular dynamics, The Journal of Chemical Physics 118 (2003) 4712–4720.
[66] E. S. Boek, J. T. Padding, W. K. den Otter, W. J. Briels, Mechanical properties of surfactant bilayer membranes from atomistic and coarse-grained molecular dynamics simulations, The Journal of Physical Chemistry B 109 (2005) 19851–19858.
[67] G. Batchelor, An Introduction to Fluid Dynamics, Cambridge Mathematical Library, Cambridge University Press, 2000.
[68] H. Lamb, Hydrodynamics, Dover, New York, 6 edition, 1945.
[69] G. V. Lau, I. J. Ford, P. A. Hunt, E. A. Müller, G. Jackson, Surface thermodynamics of planar, cylindrical, and spherical vapour-liquid interfaces of water, The Journal of Chemical Physics 142 (2015).
[70] C.-Y. Hui, A. Jagota, Surface tension, surface energy, and chemical potential due to their difference, Langmuir 29 (2013) 11310–11316.
[71] S. Knoche, J. Kierfeld, Buckling of spherical capsules, Phys. Rev. E 84 (2011) 046608.
[72] C. S. Peskin, The immersed boundary method, Acta Numerica 11 (2002) 479–517.
[73] S. Knoche, D. Vella, E. Aumaitre, P. Degen, H. Rehage, P. Cicuta, J. Kierfeld, Elastometry of deflated capsules: Elastic moduli from shape and wrinkle analysis, Langmuir 29 (2013) 12463–12471.
[74] G.-S. Jiang, C.-W. Shu, Efficient implementation of weighted ENO schemes, J. Comput. Phys. 126 (1996) 202 – 228.
[75] G.-S. Jiang, D. Peng, Weighted ENO schemes for Hamilton-Jacobi equations, SIAM J. Sci. Comput. 21 (2000) 2126–2143.
[76] A. J. Chorin, Numerical solution of the Navier-Stokes equations, Math. Comput. 22 (1968) 745–762.
[77] V. E. Henson, U. M. Yang, BoomerAMG: a parallel algebraic multigrid solver and preconditioner, Appl. Numer. Math. 41 (2000) 155–177.
[78] H. van der Vorst, Bi-CGSTAB: A fast and smoothly converging variant of Bi-CG for the solution of nonsymmetric linear systems, SIAM J. Sci. Comput. 13 (1992) 631–644.
[79] R. Falgout, J. Jones, U. Yang, The Design and Implementation of hypre, a Library of Parallel High Performance Preconditioners, Springer-Verlag, pp. 267–294.
[80] S. Balay, W. D. Gropp, L. C. McInnes, B. F. Smith, Efficient management of parallelism in object-oriented numerical software libraries, in: A. Bruaset, E. Arge, H. Langtangen (Eds.), Modern Software Tools for Scientific Computing, Springer, 1997, pp. 163–202.
[81] M. Kang, R. Fedkiw, X.-D. Liu, A boundary condition capturing method for multiphase incompressible flow, Journal of Scientific Computing 15 (2000) 323–360.
[82] S. Gottlieb, D. I. Ketcheson, C.-W. Shu, High order strong stability preserving time discretizations, J. Sci. Comput. 38

(2009) 251–289.
[83] J. Guermond, P. Minev, J. Shen, An overview of projection methods for incompressible flows, Comput. Meth. Appl. Mech. Eng. 195 (2006) 6011 – 6045.
[84] K. E. Teigen, S. T. Munkejord, Sharp-interface simulations of drop deformation in electric fields, IEEE T. Dielect. El. In. 16 (2009) 475–482.
[85] K. E. Teigen, K. Y. Lervåg, S. T. Munkejord, Sharp interface simulations of surfactant-covered drops in electric fields, in: Fifth European Conference on Computational Fluid Dynamics, ECCOMAS CFD 2010.
[86] K. E. Teigen, S. T. Munkejord, Influence of surfactant on drop deformation in an electric field, Phys. Fluids 22 (2010) –.
[87] Å. Ervik, K. Y. Lervåg, S. T. Munkejord, A robust method for calculating interface curvature and normal vectors using an extracted local level set, Journal of Computational Physics 257, Part A (2014) 259 – 277.
[88] Å. Ervik, S. M. Hellesø, S. T. Munkejord, B. Müller, Experimental and computational studies of water drops falling through model oil with surfactant and subjected to an electric field, in: Proceedings of the IEEE 18th International Conference on Dielectric Liquids, Bled, Slovenia.
[89] Å. Ervik, T. E. Penne, S. M. Hellesø, S. T. Munkejord, B. Müller, Influence of surfactants on the electrohydrodynamic stretching of water drops in oil, Submitted (2016).
[90] M. O. Lysgaard, Development of an immersed boundary method for simulating contaminated fluid interfaces in two-phase flow, Master's thesis, Department of Mathematics, Norwegian University of Science and Technology, 2015.
[91] S. Osher, J. A. Sethian, Fronts propagating with curvature-dependent speed: Algorithms based on Hamilton-Jacobi formulations, Journal of Computational Physics 79 (1988) 12 – 49.
[92] D. Adalsteinsson, J. Sethian, A fast level set method for propagating interfaces, Journal of Computational Physics 118 (1995) 269–277. Cited By 0.
[93] V. Sabelnikov, A. Y. Ovsyannikov, M. Gorokhovski, Modified level set equation and its numerical assessment, Journal of Computational Physics 278 (2014) 1 – 30.
[94] S. Osher, R. Fedkiw, Level Set Methods and Dynamic Implicit Surfaces, Applied Mathematical Sciences, Springer New York, 2012.
[95] R. P. Fedkiw, T. Aslam, B. Merriman, S. Osher, A non-oscillatory Eulerian approach to interfaces in multimaterial flows (the ghost fluid method), J. Comput. Phys. 152 (1999) 457–492.
[96] R. J. LeVeque, Z. Li, Immersed interface methods for Stokes flow with elastic boundaries or surface tension, SIAM J. Sci. Comput. 18 (1997) 709–735.
[97] J. Brackbill, D. B. Kothe, C. Zemach, A continuum method for modeling surface tension, J. Comput. Phys. 100 (1992) 335–354.
[98] C. Peskin, Numerical analysis of blood flow in the heart, Journal of Computational Physics 25 (1977) 220–252. Cited By 1276.
[99] K. Y. Lervåg, Calculation of interface curvatures with the level-set method for two-phase flow simulations and a second-order diffuse-domain method for elliptic problems in complex geometries, Ph.D. thesis, Norwegian University of Science and Technology, Faculty of Engineering Science and Technology, Department of Energy and Process Engineering, 2013.
[100] M. Sussman, E. G. Puckett, A coupled level set and volume-of-fluid method for computing 3D and axisymmetric incompressible two-phase flows, Journal of Computational Physics 162 (2000) 301–337.
[101] M. Francois, W. Shyy, Computations of drop dynamics with the immersed boundary method, part 1: numerical algorithm and buoyancy-induced effect, Numerical Heat Transfer, Part B: Fundamentals 44 (2003) 101–118.
[102] M. Uhlmann, An immersed boundary method with direct forcing for the simulation of particulate flows, Journal of Computational Physics 209 (2005) 448–476.
[103] C. Tu, C. S. Peskin, Stability and instability in the computation of flows with moving immersed boundaries: A comparison of three methods, SIAM Journal on Scientific and Statistical Computing 13 (1992) 1361–1376.
[104] C. Peskin, D. McQueen, A general method for the computer simulation of biological systems interacting with fluids, in: Symposia of the society for Experimental Biology, volume 49, pp. 265–276. Cited By 58.
[105] J. Lucassen, Longitudinal capillary waves. Part 1. Theory, Transactions of the Faraday Society 64 (1968) 2221–2229.
[106] J. Lucassen, Longitudinal capillary waves. Part 2. Experiments, Transactions of the Faraday Society 64 (1968) 2230–2235.
[107] P. Angot, C.-H. Bruneau, P. Fabrie, A penalization method to take into account obstacles in incompressible viscous flows, Numerische Mathematik 81 (1999) 497–520.
[108] M. Kang, R. P. Fedkiw, X.-D. Liu, A boundary condition capturing method for multiphase incompressible flow, Journal of Scientific Computing 15 (2000) 323–360.
[109] R. J. Leveque, High-resolution conservative algorithms for advection in incompressible flow, SIAM Journal on Numerical Analysis 33 (1996) pp. 627–665.
[110] S. T. Zalesak, Fully multidimensional flux-corrected transport algorithms for fluids, Journal of Computational Physics 31 (1979) 335 – 362.
[111] O. Lobanova, A. Mejía, G. Jackson, E. A. Müller, SAFT-$\gamma$ force field for the simulation of molecular fluids 6: Binary and ternary mixtures comprising water, carbon dioxide, and n-alkanes, The Journal of Chemical Thermodynamics 93 (2016) 320 – 336.
[112] J. Saien, , S. Akbari, Interfacial tension of toluene + water + sodium dodecyl sulfate from 20 to 50 °C and pH between 4 and 9, Journal of Chemical & Engineering Data 51 (2006) 1832–1835.
[113] H. W. Yarranton, J. H. Masliyah, Gibbs-Langmuir model for interfacial tension of nonideal organic mixtures over water, The Journal of Physical Chemistry 100 (1996) 1786–1792.
[114] S. Zeppieri, J. Rodríguez, A. L. L. de Ramos, Interfacial tension of alkane + water systems, Journal of Chemical & Engineering Data 46 (2001) 1086–1088.

[115] E. Rogel, L. Carbognani, Density estimation of asphaltenes using molecular dynamics simulations, Energy & fuels 17 (2003) 378–386.
[116] J. Pacheco-Sánchez, I. Zaragoza, J. Martínez-Magadán, Asphaltene aggregation under vacuum at different temperatures by molecular dynamics, Energy & fuels 17 (2003) 1346–1355.
[117] S. R. Stoyanov, S. Gusarov, A. Kovalenko, Multiscale modelling of asphaltene disaggregation, Molecular Simulation 34 (2008) 953–960.
[118] T. Kuznicki, J. H. Masliyah, S. Bhattacharjee, Aggregation and partitioning of model asphaltenes at toluene- water interfaces: Molecular dynamics simulations, Energy & Fuels 23 (2009) 5027–5035.
[119] T. F. Headen, E. S. Boek, N. T. Skipper, Evidence for asphaltene nanoaggregation in toluene and heptane from molecular dynamics simulations, Energy & Fuels 23 (2009) 1220–1229.
[120] E. S. Boek, D. S. Yakovlev, T. F. Headen, Quantitative molecular representation of asphaltenes and molecular dynamics simulation of their aggregation, Energy & Fuels 23 (2009) 1209–1219.
[121] T. F. Headen, E. S. Boek, Molecular dynamics simulations of asphaltene aggregation in supercritical carbon dioxide with and without limonene, Energy & Fuels 25 (2010) 503–508.
[122] M. Sedghi, L. Goual, W. Welch, J. Kubelka, Effect of asphaltene structure on association and aggregation using molecular dynamics, The Journal of Physical Chemistry B 117 (2013) 5765–5776.
[123] P. Ungerer, D. Rigby, B. Leblanc, M. Yiannourakou, Sensitivity of the aggregation behaviour of asphaltenes to molecular weight and structure using molecular dynamics, Molecular Simulation 40 (2014) 115–122.
[124] Y. Mikami, Y. Liang, T. Matsuoka, E. S. Boek, Molecular dynamics simulations of asphaltenes at the oil–water interface: from nanoaggregation to thin-film formation, Energy & Fuels 27 (2013) 1838–1845.
[125] J. Liu, Y. Zhao, S. Ren, Molecular dynamics simulation of self-aggregation of asphaltenes at an oil/water interface: formation and destruction of the asphaltene protective film, Energy & Fuels 29 (2015) 1233–1242.
[126] F. Yang, P. Tchoukov, H. Dettman, R. B. Teklebrhan, L. Liu, T. Dabros, J. Czarnecki, J. Masliyah, Z. Xu, Asphaltene subfractions responsible for stabilizing water-in-crude oil emulsions. Part 2: Molecular representations and molecular dynamics simulations, Energy & Fuels 29 (2015) 4783–4794.
[127] Y. Ruiz-Morales, O. C. Mullins, Coarse-grained molecular simulations to investigate asphaltenes at the oil–water interface, Energy & Fuels 29 (2015) 1597–1609.
[128] D. Fenistein, L. Barre, Experimental measurement of the mass distribution of petroleum asphaltene aggregates using ultracentrifugation and small-angle X-ray scattering, Fuel 80 (2001) 283–287.
[129] N. H. Rahmani, T. Dabros, J. H. Masliyah, Fractal structure of asphaltene aggregates, Journal of colloid and interface science 285 (2005) 599–608.
[130] N. V. Lisitza, D. E. Freed, P. N. Sen, Y.-Q. Song, Study of asphaltene nanoaggregation by nuclear magnetic resonance (NMR), Energy & Fuels 23 (2009) 1189–1193.
[131] O. C. Mullins, H. Sabbah, J. Eyssautier, A. E. Pomerantz, L. Barré, A. B. Andrews, Y. Ruiz-Morales, F. Mostowfi, R. McFarlane, L. Goual, et al., Advances in asphaltene science and the Yen–Mullins model, Energy & Fuels 26 (2012) 3986–4003.
[132] J. D. McLean, P. K. Kilpatrick, Effects of asphaltene aggregation in model heptane-toluene mixtures on stability of water-in-oil emulsions, Journal of Colloid and Interface Science 196 (1997) 23 – 34.
[133] J. Djuve, X. Yang, J. I. Fjellanger, J. Sjöblom, E. Pelizzetti, Chemical destabilization of crude oil based emulsions and asphaltene stabilized emulsions, Colloid and Polymer Science 279 (2001) 232–239.
[134] P. Spiecker, K. L. Gawrys, C. B. Trail, P. K. Kilpatrick, Effects of petroleum resins on asphaltene aggregation and water-in-oil emulsion formation, Colloids and Surfaces A: Physicochemical and Engineering Aspects 220 (2003) 9 – 27.
[135] P. Spiecker, K. L. Gawrys, P. K. Kilpatrick, Aggregation and solubility behavior of asphaltenes and their subfractions, Journal of Colloid and Interface Science 267 (2003) 178 – 193.
[136] P. M. Spiecker, P. K. Kilpatrick, Interfacial rheology of petroleum asphaltenes at the oil-water interface, Langmuir 20 (2004) 4022–4032.
[137] H. Yarranton, D. Sztukowski, P. Urrutia, Effect of interfacial rheology on model emulsion coalescence: I. Interfacial rheology, Journal of Colloid and Interface Science 310 (2007) 246 – 252.
[138] S. Wang, J. Liu, L. Zhang, J. Masliyah, Z. Xu, Interaction forces between asphaltene surfaces in organic solvents, Langmuir 26 (2010) 183–190.
[139] D. M. Sztukowski, H. W. Yarranton, Rheology of asphaltene-toluene/water interfaces, Langmuir 21 (2005) 11651–11658.
[140] K. Norinaga, V. J. Wargardalam, S. Takasugi, M. Iino, , S. Matsukawa, Measurement of self-diffusion coefficient of asphaltene in pyridine by pulsed field gradient spin-echo 1H NMR, Energy & Fuels 15 (2001) 1317–1318.
[141] A. B. Andrews, A. McClelland, O. Korkeila, A. Demidov, A. Krummel, O. C. Mullins, Z. Chen, Molecular orientation of asphaltenes and PAH model compounds in langmuir-blodgett films using sum frequency generation spectroscopy, Langmuir 27 (2011) 6049–6058.
[142] M. Fossen, H. Kallevik, K. D. Knudsen, J. Sjöblom, Asphaltenes precipitated by a two-step precipitation procedure. 1. Interfacial tension and solvent properties, Energy & Fuels 21 (2007) 1030–1037.
[143] V. J. Verruto, R. K. Le, P. K. Kilpatrick, Adsorption and molecular rearrangement of amphoteric species at oil-water interfaces, The Journal of Physical Chemistry B 113 (2009) 13788–13799.
[144] Y. Fan, S. Simon, J. Sjöblom, Interfacial shear rheology of asphaltenes at oil–water interface and its relation to emulsion stability: influence of concentration, solvent aromaticity and nonionic surfactant, Colloids and Surfaces A: Physicochemical and Engineering Aspects 366 (2010) 120–128.
[145] K. Kumar, A. Nikolov, D. Wasan, Mechanisms of stabilization of water-in-crude oil emulsions, Industrial & engineering chemistry research 40 (2001) 3009–3014.

[146] N. Aske, R. Orr, J. Sjöblom, Dilatational elasticity moduli of water–crude oil interfaces using the oscillating pendant drop, Journal of dispersion science and technology 23 (2002) 809–825.
[147] D. Daniel-David, I. Pezron, C. Dalmazzone, C. Noïk, D. Clausse, L. Komunjer, Elastic properties of crude oil/water interface in presence of polymeric emulsion breakers, Colloids and Surfaces A: Physicochemical and Engineering Aspects 270 (2005) 257–262.
[148] A. F. Barton, Handbook of Solubility Parameters, CRC Press, 1983.
[149] S. Li, V. R. Cooper, T. Thonhauser, A. Puzder, D. C. Langreth, A density functional theory study of the benzene-water complex, The Journal of Physical Chemistry A 112 (2008) 9031–9036.

## Appendix A. Parameters for the continuum simulation cases

Table A.1: Parameters for the drop in potential vortex.

| Parameter | Symbol | Value |
|---|---|---|
| Drop radius | $r$ | 0.15 |
| Domain size | $\Omega$ | $1 \times 1$ |
| Stability safety factor | $C$ | 0.5 |
| Euler grid nodes | $N$ | $200 \times 200$ |
| Lagrangian point density | | $5/\Delta$ |

Table A.2: Parameters for the Zalesak's disk test.

| Parameter | Symbol | Value |
|---|---|---|
| Disk radius | $r$ | $1/3$ |
| Domain size | $\Omega$ | $1 \times 1$ |
| Time step safety factor | $C$ | 0.5 |
| Euler grid nodes | $N$ | $64 \times 64$ |
| Velocity field | $\mathbf{u}$ | $\frac{\pi}{10}[1/2 - y, x - 1/2]$ |
| Lagrangian point density | | $5/\Delta$ |

Table A.3: Parameters for the elliptical drop driven by interfacial tension.

| Parameter | Symbol | Value |
|---|---|---|
| Drop density | $\rho_1$ | $10^3\,\mathrm{kg/m^3}$ |
| Matrix density | $\rho_2$ | $10^3\,\mathrm{kg/m^3}$ |
| Drop viscosity | $\mu_1$ | $10^{-3}\,\mathrm{Pa \cdot s}$ |
| Matrix viscosity | $\mu_2$ | $10^{-3}\,\mathrm{Pa \cdot s}$ |
| Interfacial tension | $\gamma$ | $15 \times 10^{-3}\,\mathrm{N/m}$ |
| Drop radius | $r$ | $10^{-3}\,\mathrm{m}$ |
| Drop axis length ratio | $\frac{a}{b}$ | 1.16 |
| Domain size | $\Omega$ | $0.007 \times 0.007\,\mathrm{m}$ |
| Time step safety factor | $C$ | 0.2 |
| Grid nodes | $N$ | $\{100, 200, 400, 800\}$ |

Table A.4: Parameters for relaxing drop with viscosity and density jump.

| Parameter | Symbol | Value |
|---|---|---|
| Drop density | $\rho_1$ | $10^3\,\mathrm{kg/m^3}$ |
| Matrix density | $\rho_2$ | $5 \times 10^2\,\mathrm{kg/m^3}$ |
| Drop viscosity | $\mu_1$ | $10^{-3}\,\mathrm{Pa \cdot s}$ |
| Matrix viscosity | $\mu_2$ | $10^{-2}\,\mathrm{Pa \cdot s}$ |
| Interfacial tension | $\gamma$ | $15 \times 10^{-3}\,\mathrm{N/m}$ |
| Drop radius | $r$ | $10^{-3}\,\mathrm{m}$ |
| Drop axis length ratio | $\frac{a}{b}$ | 1.16 |
| Domain size | $\Omega$ | $0.007 \times 0.007\,\mathrm{m}$ |
| Time step safety factor | $C$ | 0.2 |
| Grid nodes | $N$ | 400 |

Table A.5: Parameters for relaxing drop with an elastic membrane.

| Parameter | Symbol | Value |
|---|---|---|
| Drop density | $\rho_1$ | $10^3\,\mathrm{kg/m^3}$ |
| Matrix density | $\rho_2$ | $10^3\,\mathrm{kg/m^3}$ |
| Drop viscosity | $\mu_1$ | $10^{-3}\,\mathrm{Pa \cdot s}$ |
| Matrix viscosity | $\mu_2$ | $10^{-3}\,\mathrm{Pa \cdot s}$ |
| Interfacial tension | $\gamma$ | $15 \times 10^{-3}\,\mathrm{N/m}$ |
| Elasticity | $K_a$ | 0 and $15 \times 10^{-2}\,\mathrm{N/m}$ |
| Drop radius | $r$ | $10^{-3}\,\mathrm{m}$ |
| Drop axis length ratio | $\frac{a}{b}$ | 3.0 |
| Domain size | $\Omega$ | $0.007 \times 0.007\,\mathrm{m}$ |
| Time step safety factor | $C$ | 0.5 |
| Grid nodes | $N$ | 150 |

Table A.6: Parameters for the pendant drop case.

| Parameter | Symbol | Value |
|---|---|---|
| Drop density | $\rho_1$ | $1000\,\mathrm{kg/m^3}$ |
| Matrix density | $\rho_2$ | $830\,\mathrm{kg/m^3}$ |
| Drop viscosity | $\mu_1$ | $1.03 \times 10^{-3}\,\mathrm{Pa \cdot s}$ |
| Matrix viscosity | $\mu_2$ | $12.4 \times 10^{-3}\,\mathrm{Pa \cdot s}$ |
| Interfacial tension | $\gamma$ | $30 \times 10^{-3}\,\mathrm{N/m}$ |
| Elasticity | $K_a$ | $50 \times 10^{-3}\,\mathrm{N/m}$ |
| Drop radius | $r$ | $3.3 \times 10^{-3}\,\mathrm{m}$ |
| Domain size | $\Omega$ | $(5 \times 10^{-3}) \times (15 \times 10^{-3})\,\mathrm{m}$ |
| Time step safety factor | $C$ | 0.3 |
| Grid nodes | $N$ | $132 \times 200$ |
| Penalisation | $\eta$ | $3 \times 10^{-5}$ |

Table A.7: Parameters for the micropipette case.

| Parameter | Symbol | Value |
|---|---|---|
| Drop density | $\rho_1$ | $1000\,\mathrm{kg/m^3}$ |
| Matrix density | $\rho_2$ | $830\,\mathrm{kg/m^3}$ |
| Drop viscosity | $\mu_1$ | $1.03 \times 10^{-3}\,\mathrm{Pa \cdot s}$ |
| Matrix viscosity | $\mu_2$ | $12.4 \times 10^{-3}\,\mathrm{Pa \cdot s}$ |
| Interfacial tension | $\gamma$ | $40 \times 10^{-3}\,\mathrm{N/m}$ |
| Elasticity | $K_a$ | $50 \times 10^{-3}\,\mathrm{N/m}$ |
| Drop radius | $r$ | $1 \times 10^{-3}\,\mathrm{m}$ |
| Domain size | $\Omega$ | $(2 \times 10^{-3}) \times (3 \times 10^{-3})\,\mathrm{m}$ |
| Time step safety factor | $C$ | 0.5 |
| Grid nodes | $N$ | $132 \times 200$ |
| Penalisation | $\eta$ | $5 \times 10^{-6}$ |

## Appendix B. Parameters and scripts for the molecular simulations

The molecular simulations reported here are performed using our raaSAFT framework. Scripts which can be used to reproduce the molecular simulations are available in the `replication` directory of the raaSAFT repository, at `http://www.bitbucket.org/asmunder/raasaft`. The force field parameters are mostly published elsewhere, as indicated by the DOI for each model in that repository. However, the force field parameters for the aromatic beads used in the APCE and APCL asphaltene models have not been published elsewhere yet. These are given in Table B.8. The parameters for the toluene model are also not published elsewhere yet, these are given in Table B.8.

Table B.8: Parameters for the aromatic beads.

| Parameter | Value | Unit |
|---|---|---|
| | **Toluene** | |
| $\epsilon/k_B$ | 269.74 | [K] |
| $\sigma$ | 3.6794 | [Å] |
| $n$ | 11.804 | [-] |
| $m$ | 6 | [-] |
| | **APCE** | |
| $\epsilon/k_B$ | 312.90 | [K] |
| $\sigma$ | 3.975 | [Å] |
| $n$ | 10 | [-] |
| $m$ | 6 | [-] |